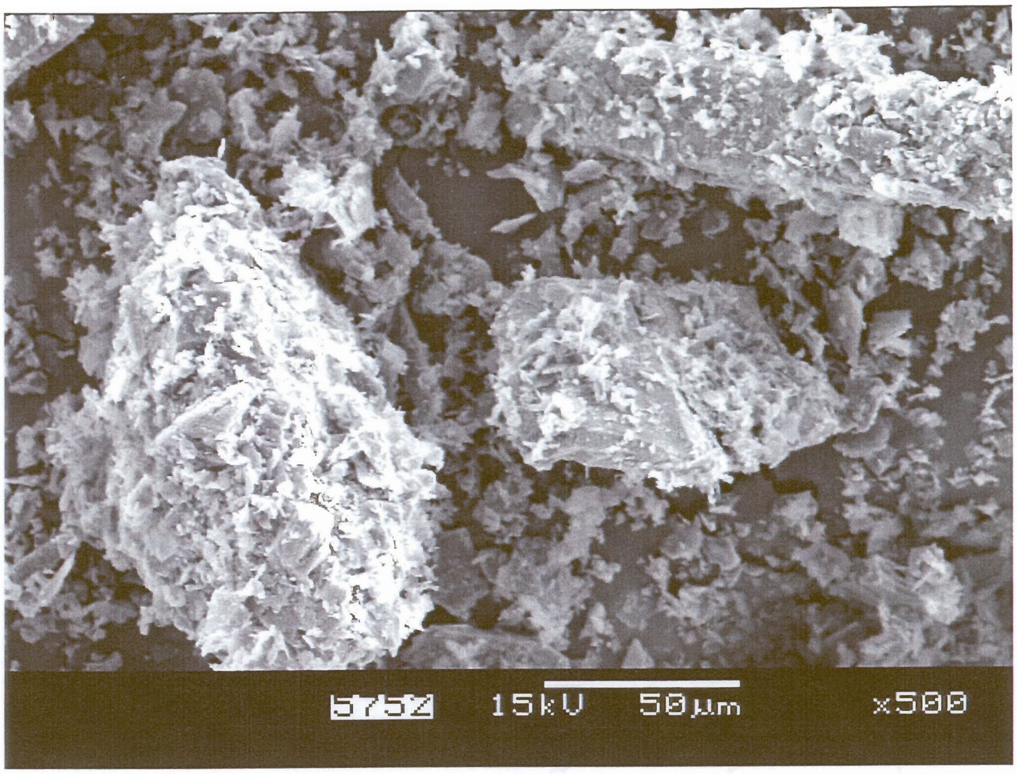


(a)

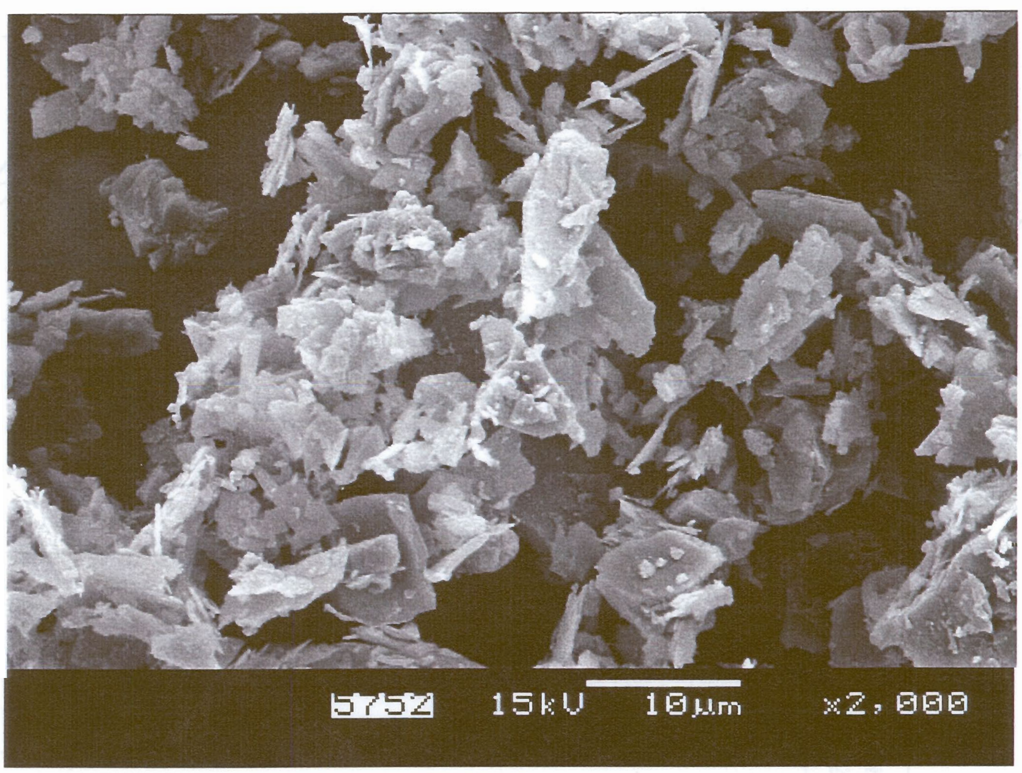


(b)

**Figure 4-1: Evidence of flocculation of the flaky slimes (a) onto coarser sand grains, and (b) into flocs of slimes.**

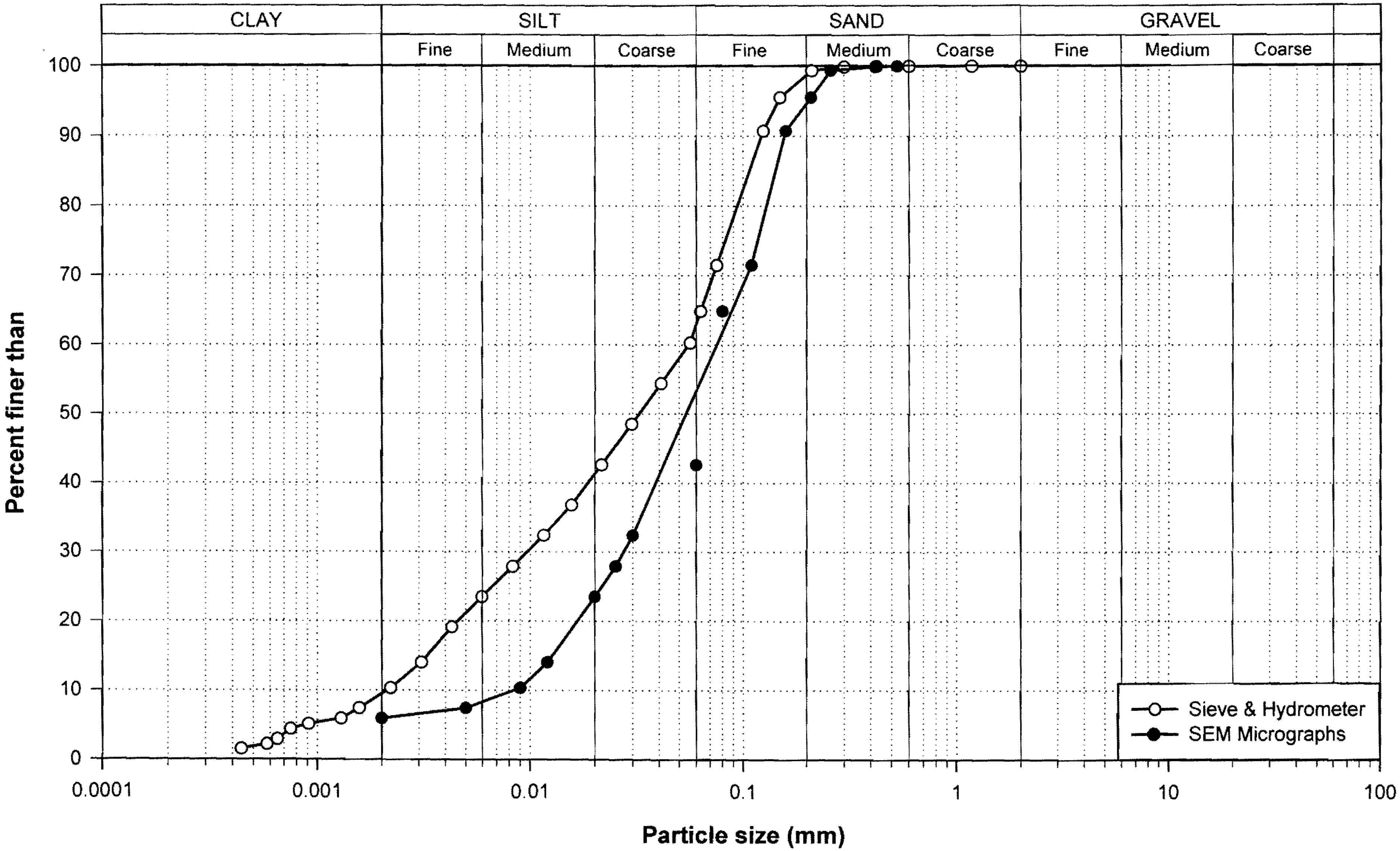


**Figure 4-2: Mizpah Whole Tailings: Grading by sieve and sedimentation tests compared with the grading derived from SEM micrographs.**

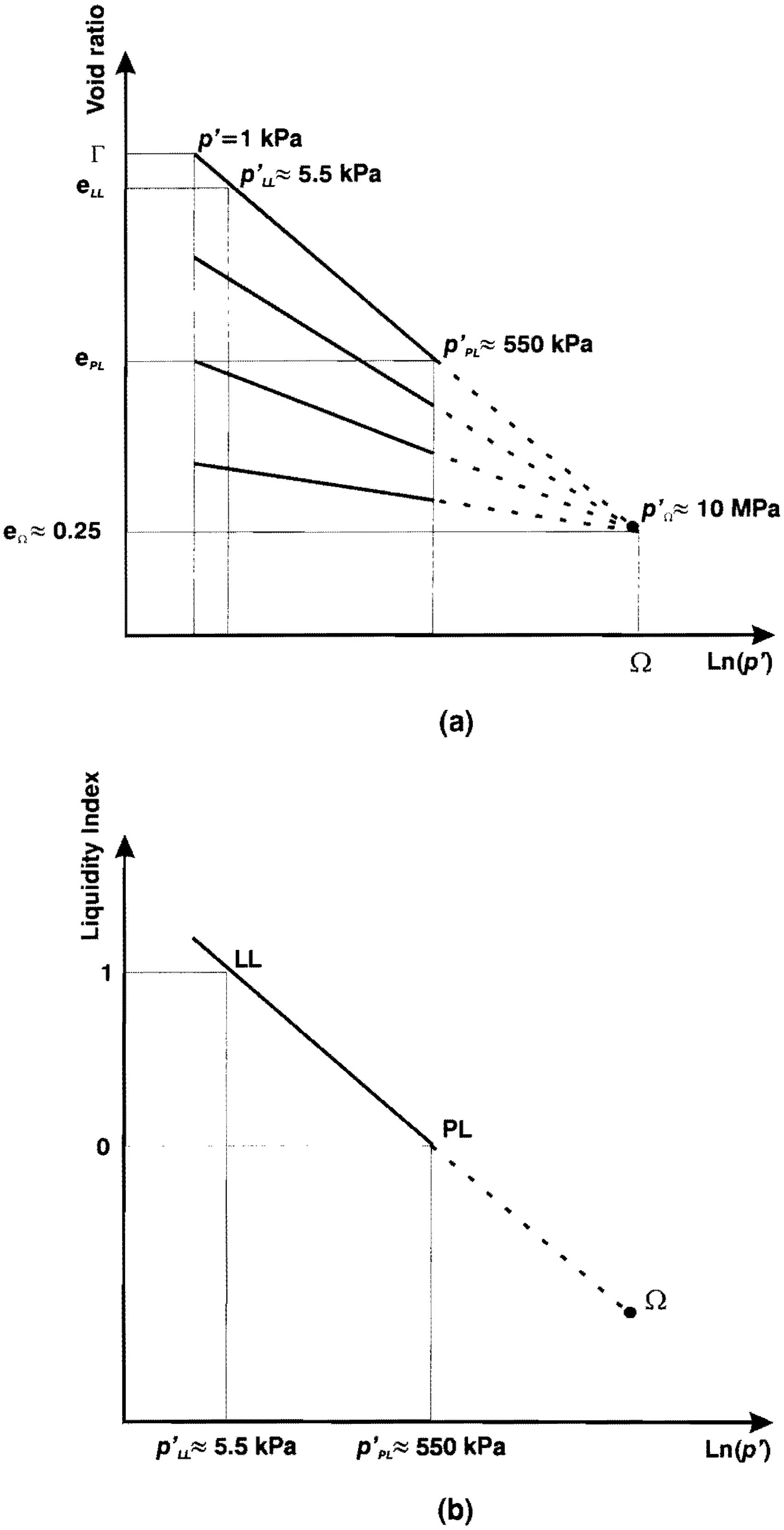


**Figure 4-3: (a) Idealised family of Critical State Lines, (b) Normalised Critical State Line (Schofield & Wroth, 1968).**

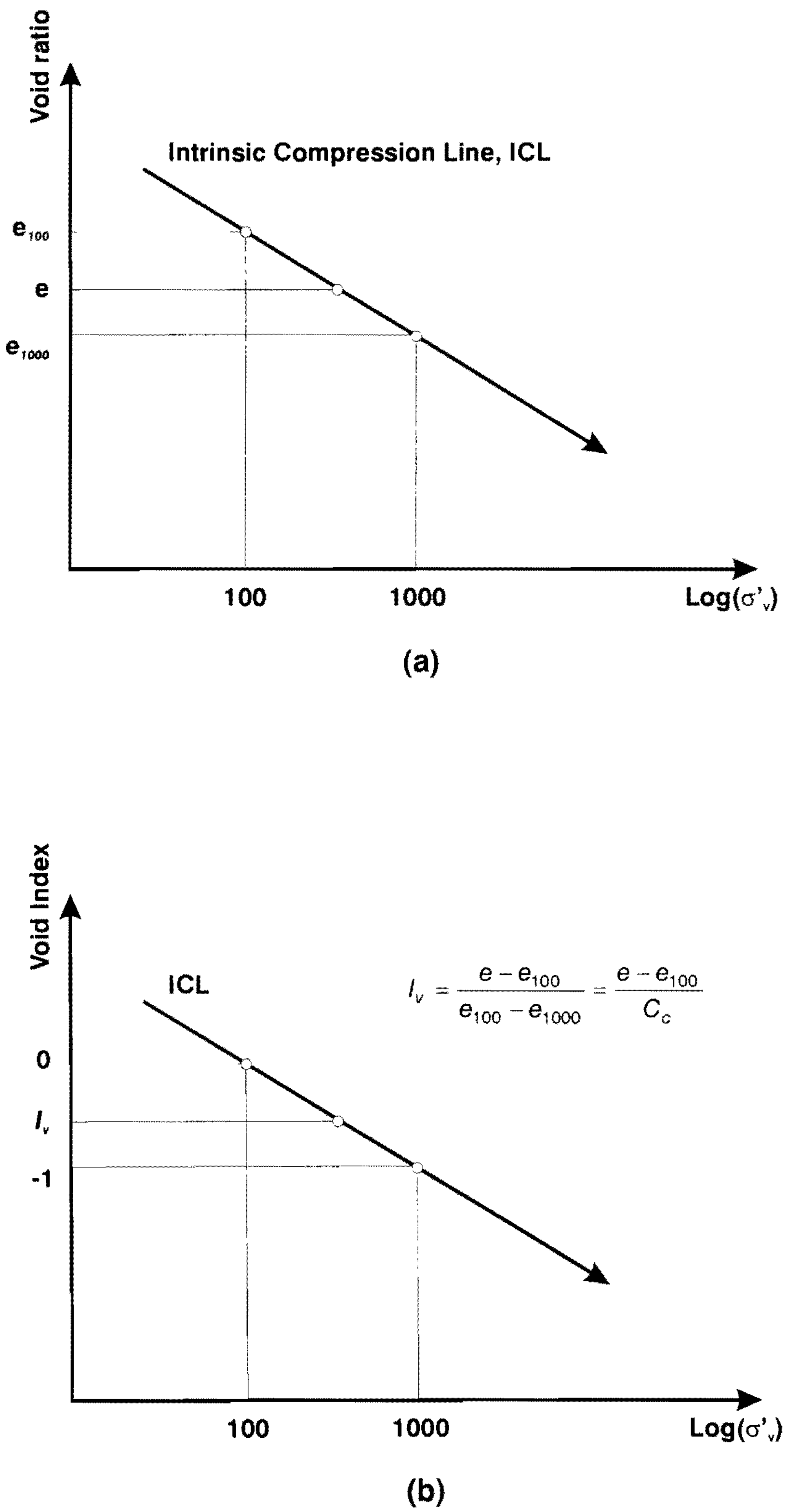


**Figure 4-4: Use of the Void Index, $I_v$, to normalise compression data (Burland, 1990).**

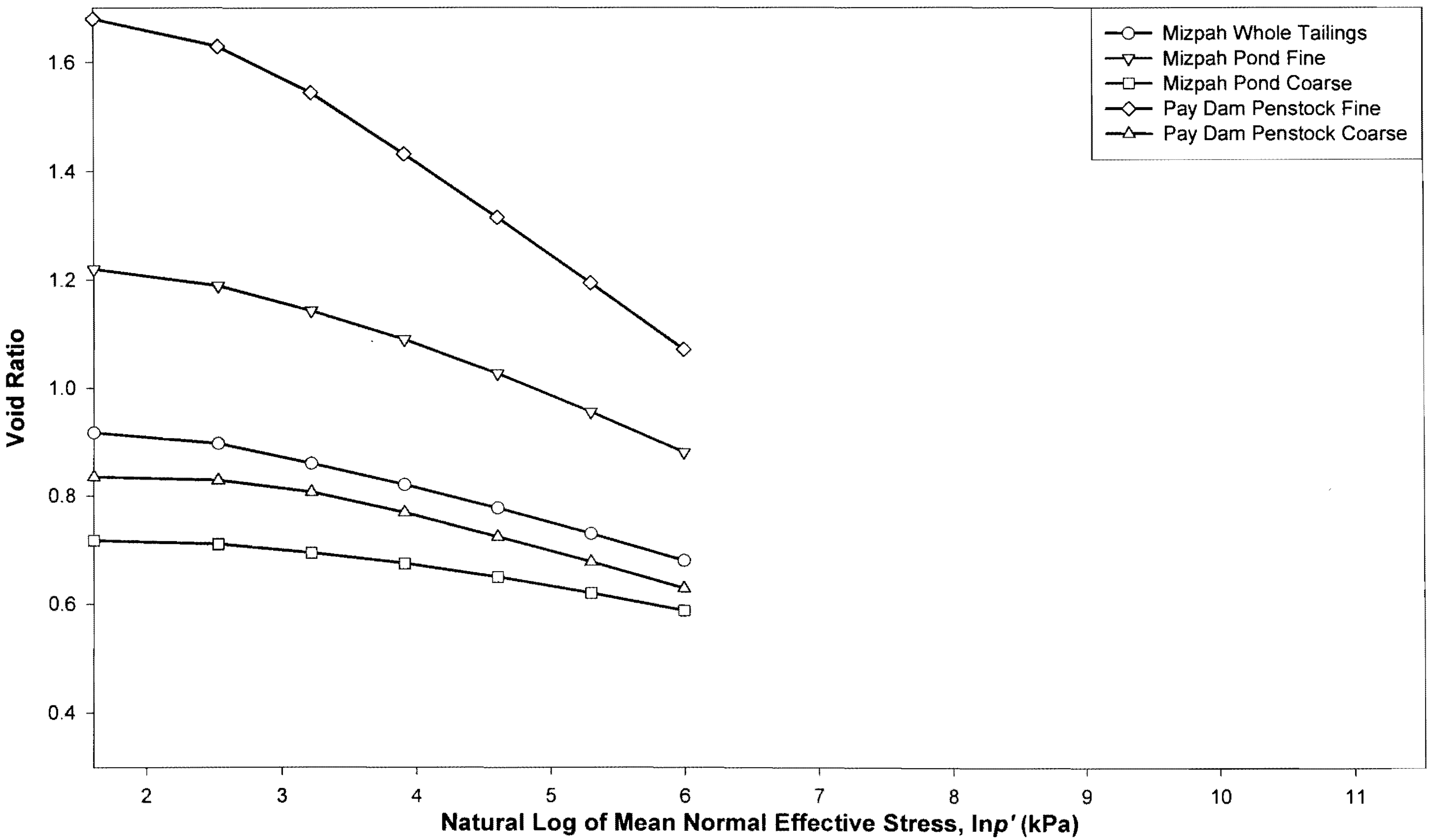


**Figure 4-5: Isotropic compression behaviour of the tailings considered in this study.**

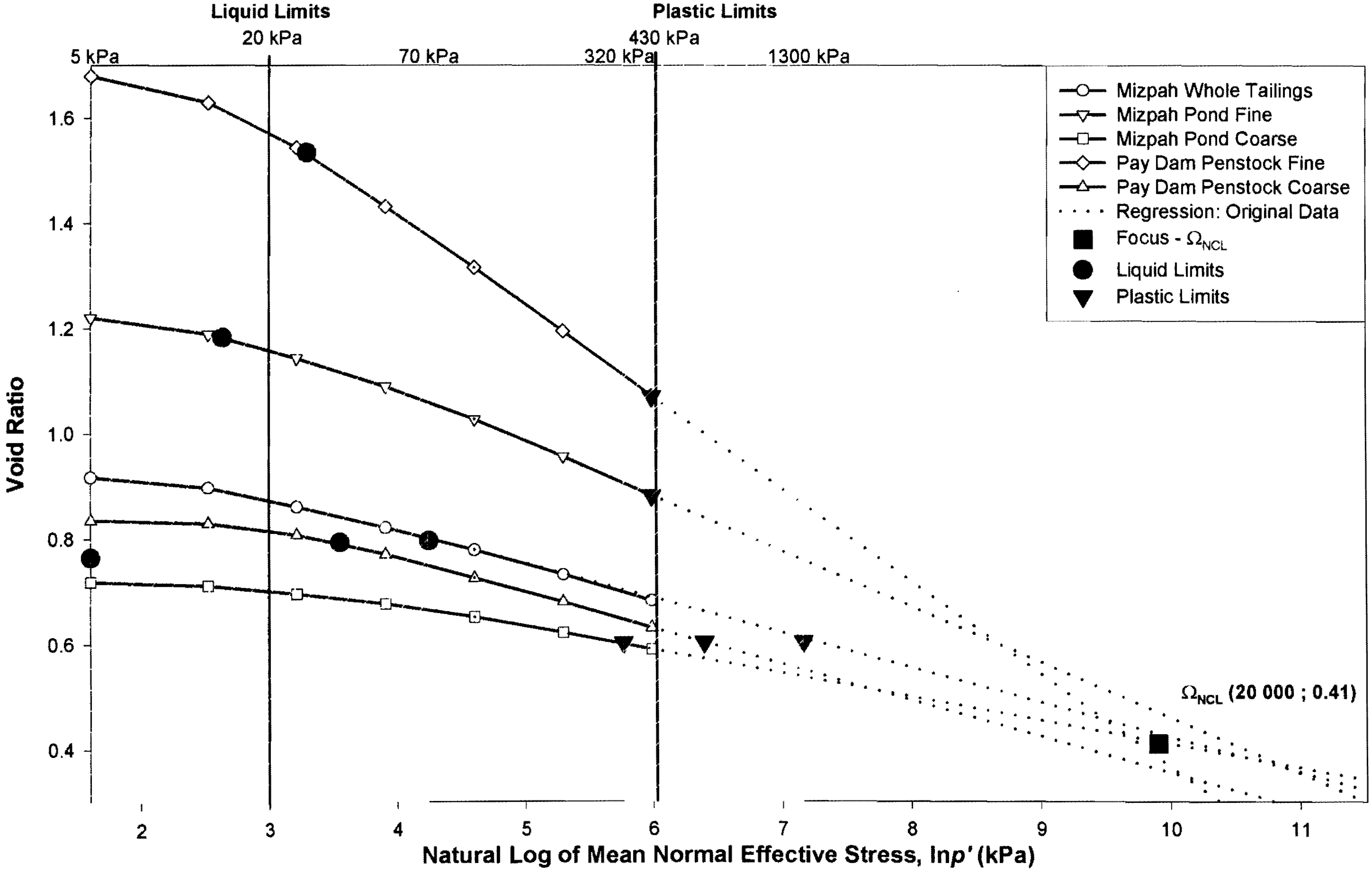


Figure 4-6: Geometric extrapolation of the compression data.

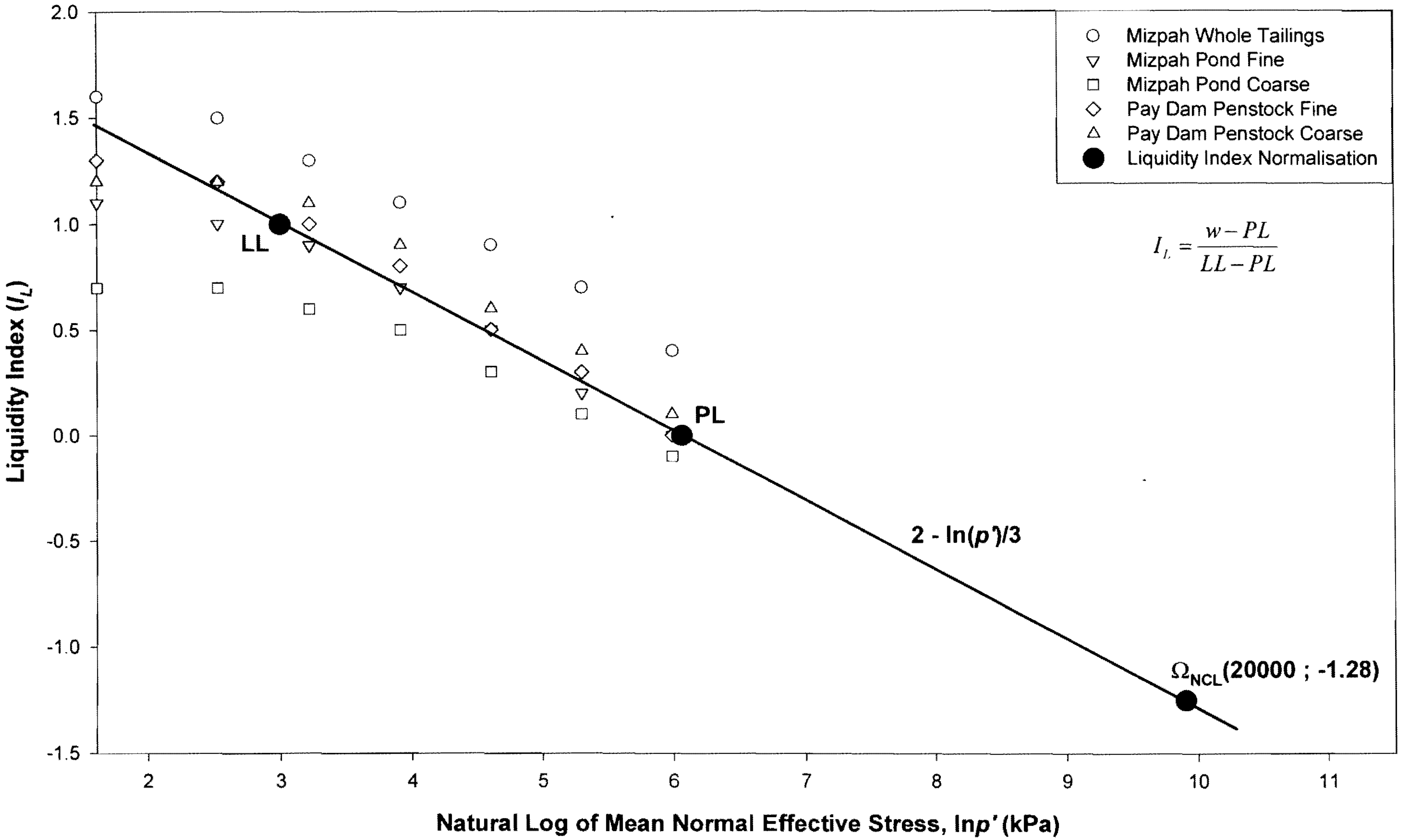


**Figure 4-7: Isotropic compression data normalised with the Liquidity Index after Schofield & Wroth (1968).**

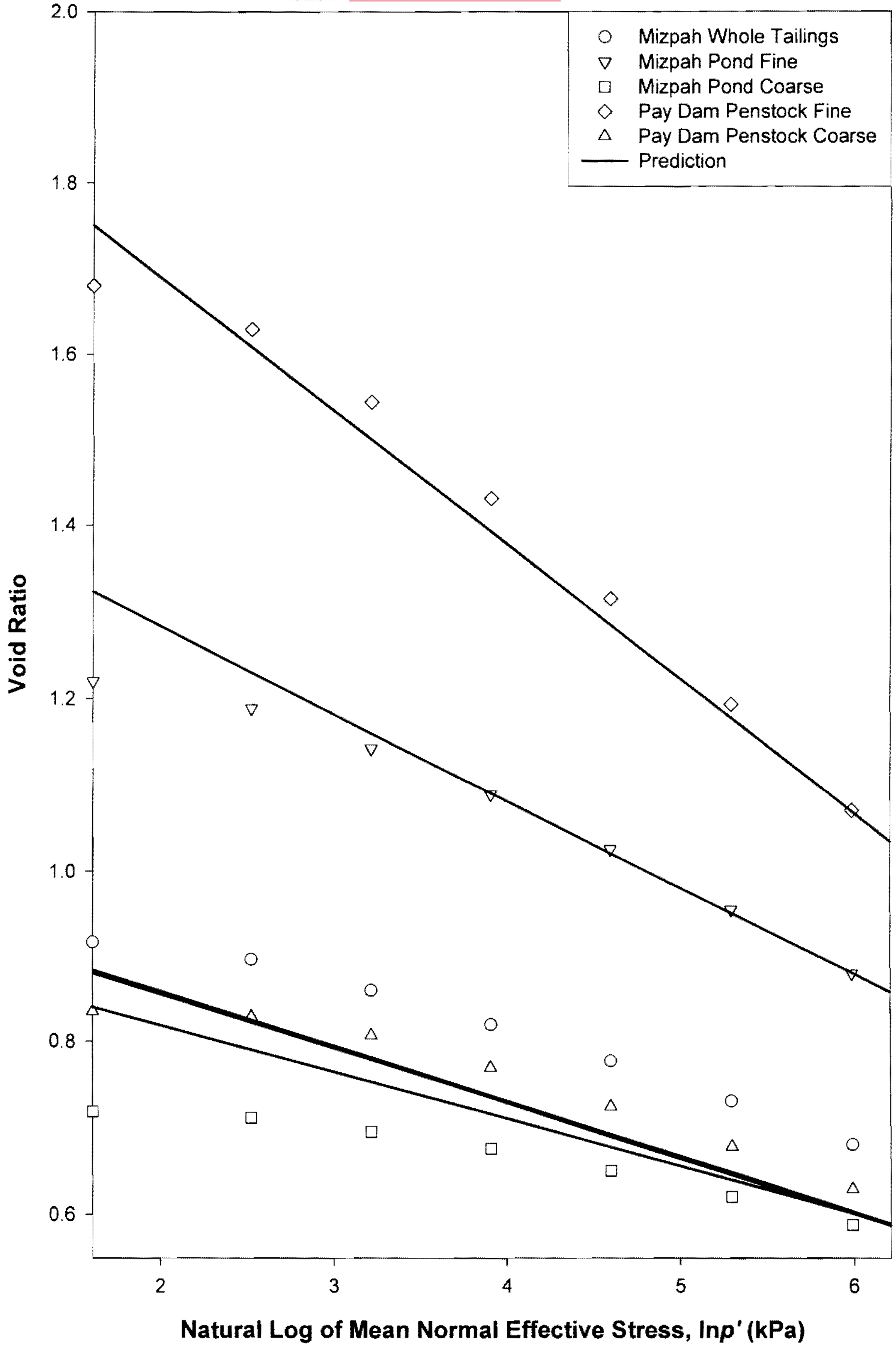


**Figure 4-8: Predicting the compression behaviour of gold tailings using $I_L$ and the Atterberg limits.**

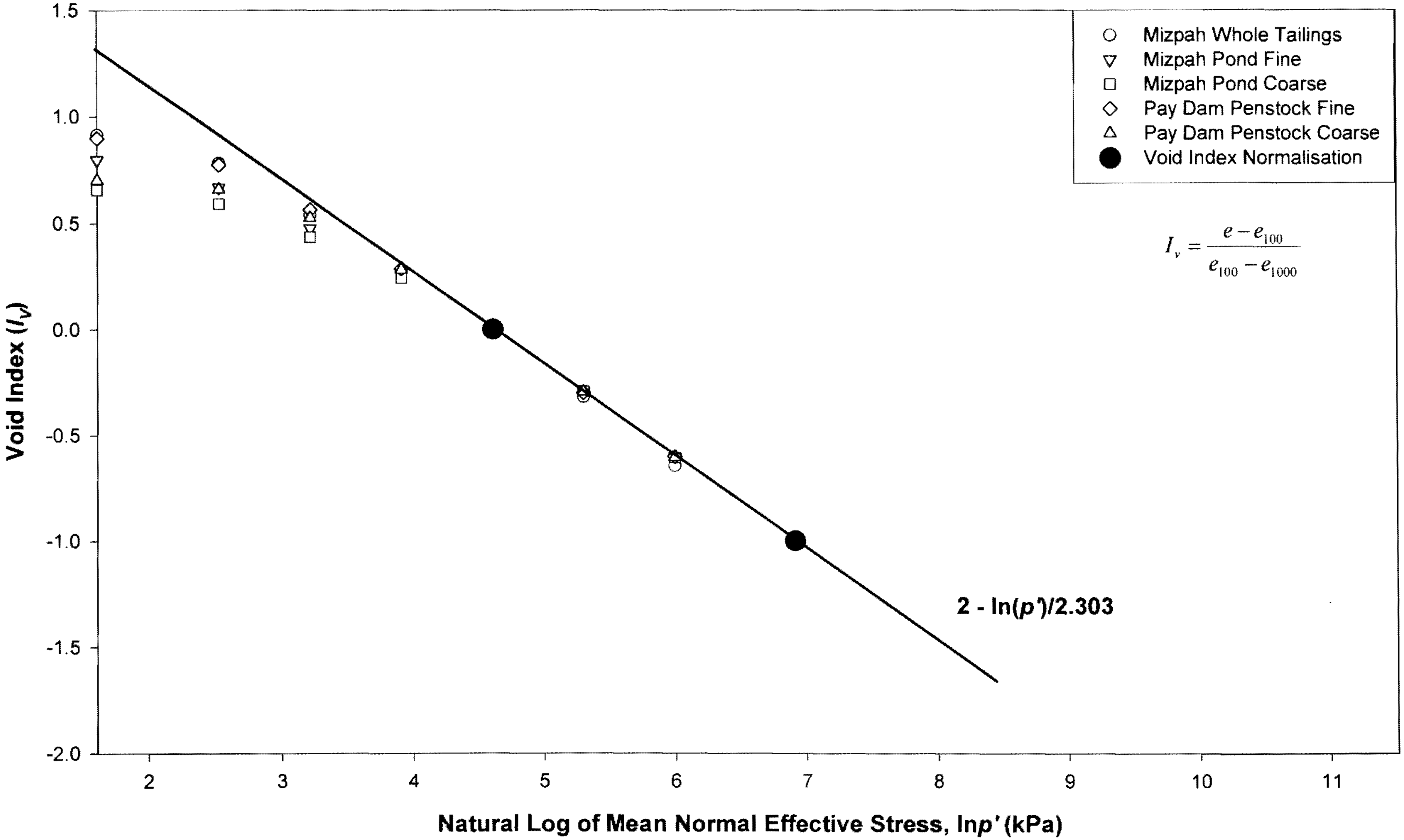


**Figure 4-9: Isotropic compression data normalised with the Void Index after Burland (1990).**

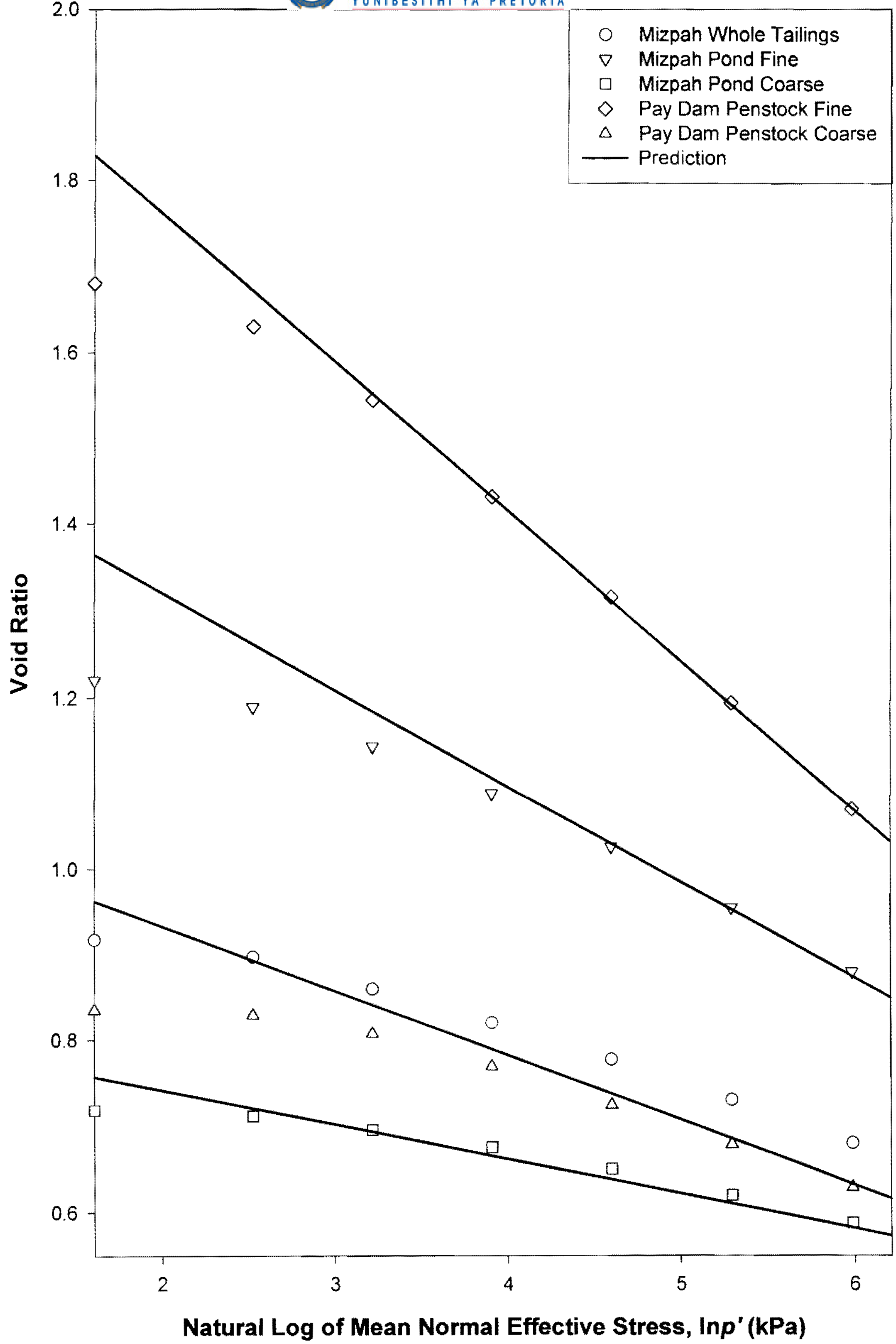


**Figure 4-10: Predicting the compression behaviour of gold tailings using $I_v$ and the Atterberg limits.**

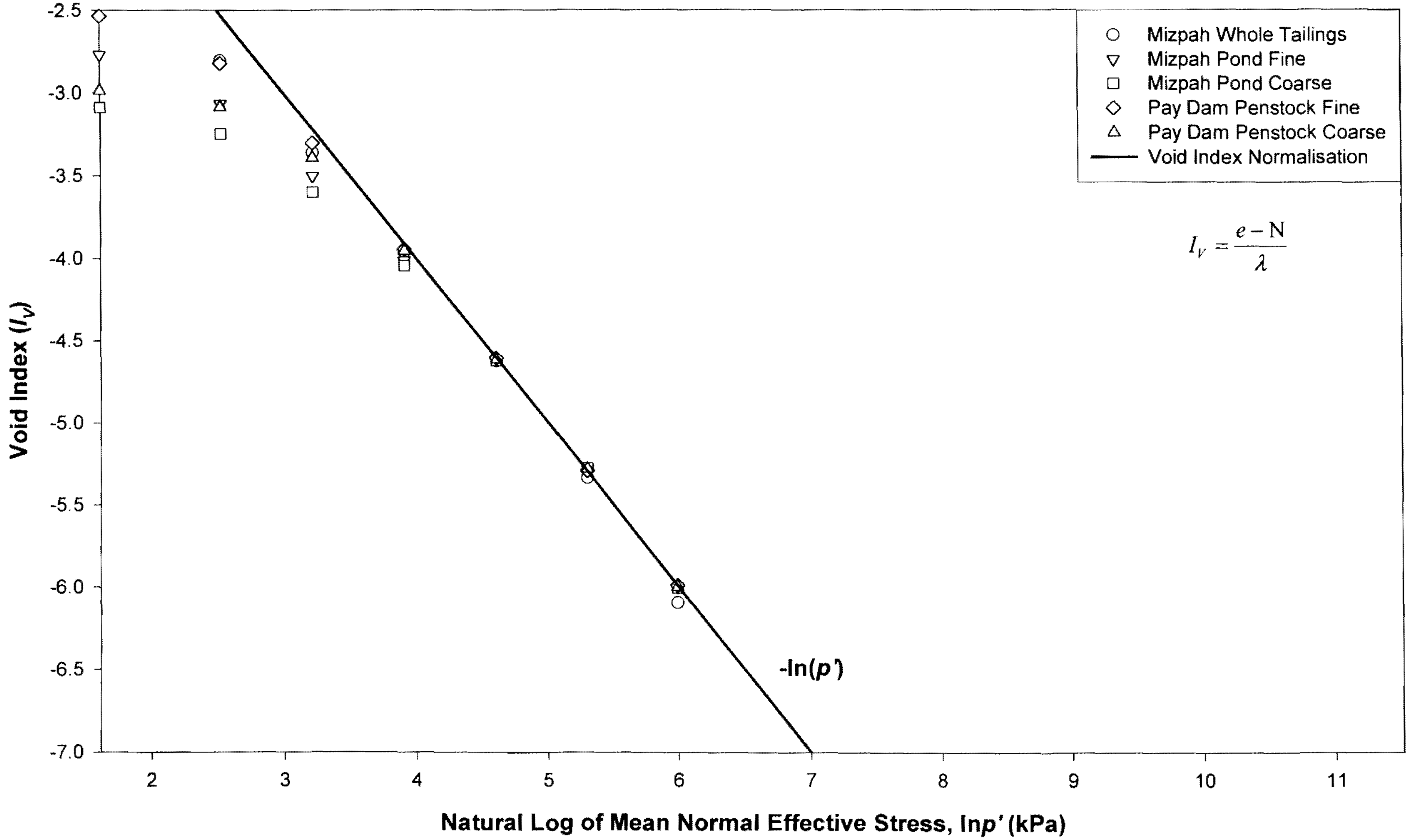


**Figure 4-11: Isotropic compression data normalised with the Void Index in terms of critical state parameters.**

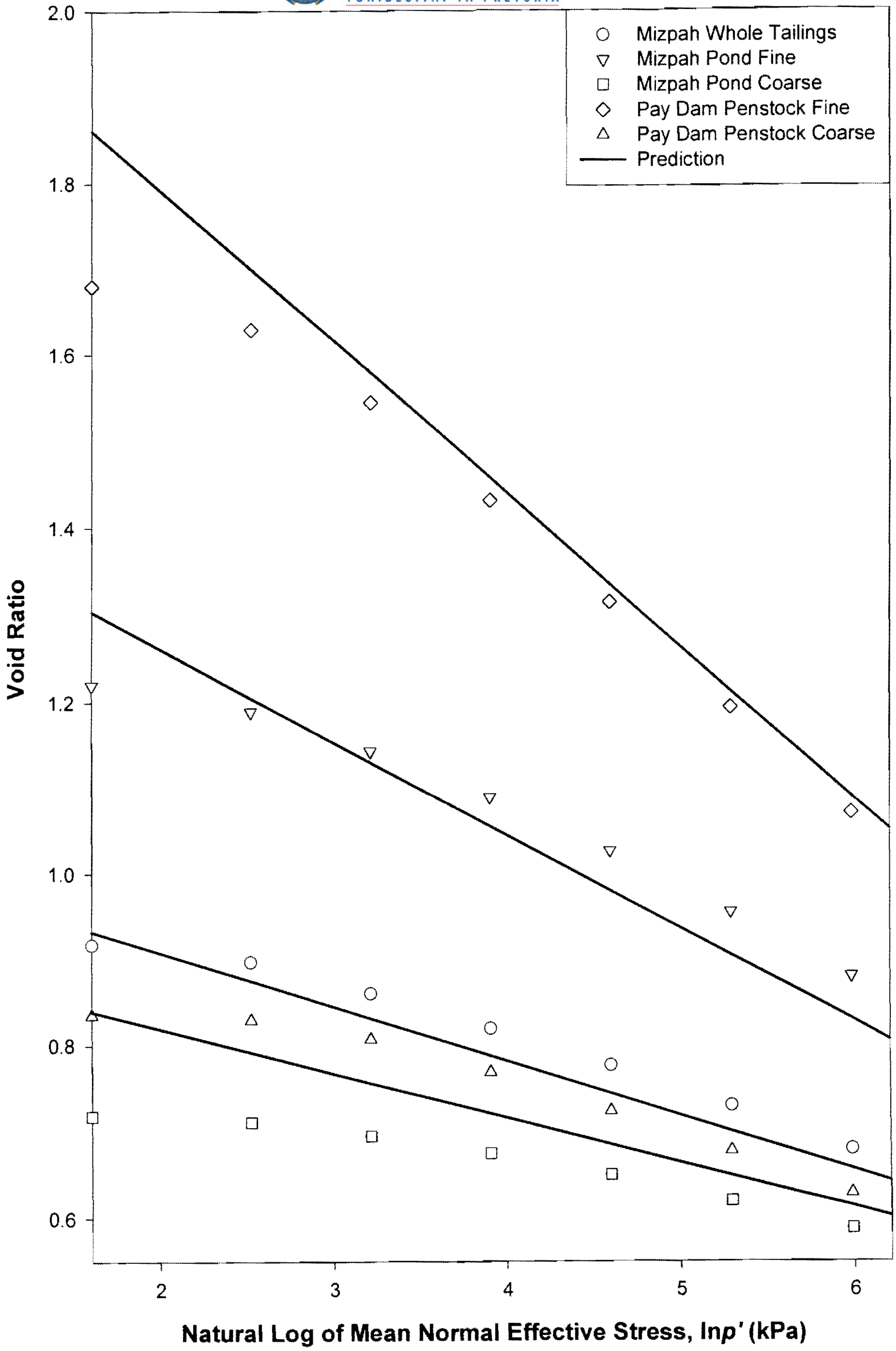


**Figure 4-12: Predicting the compression behaviour of gold tailings using empirical correlations between CSSM-parameters and the Atterberg limits.**

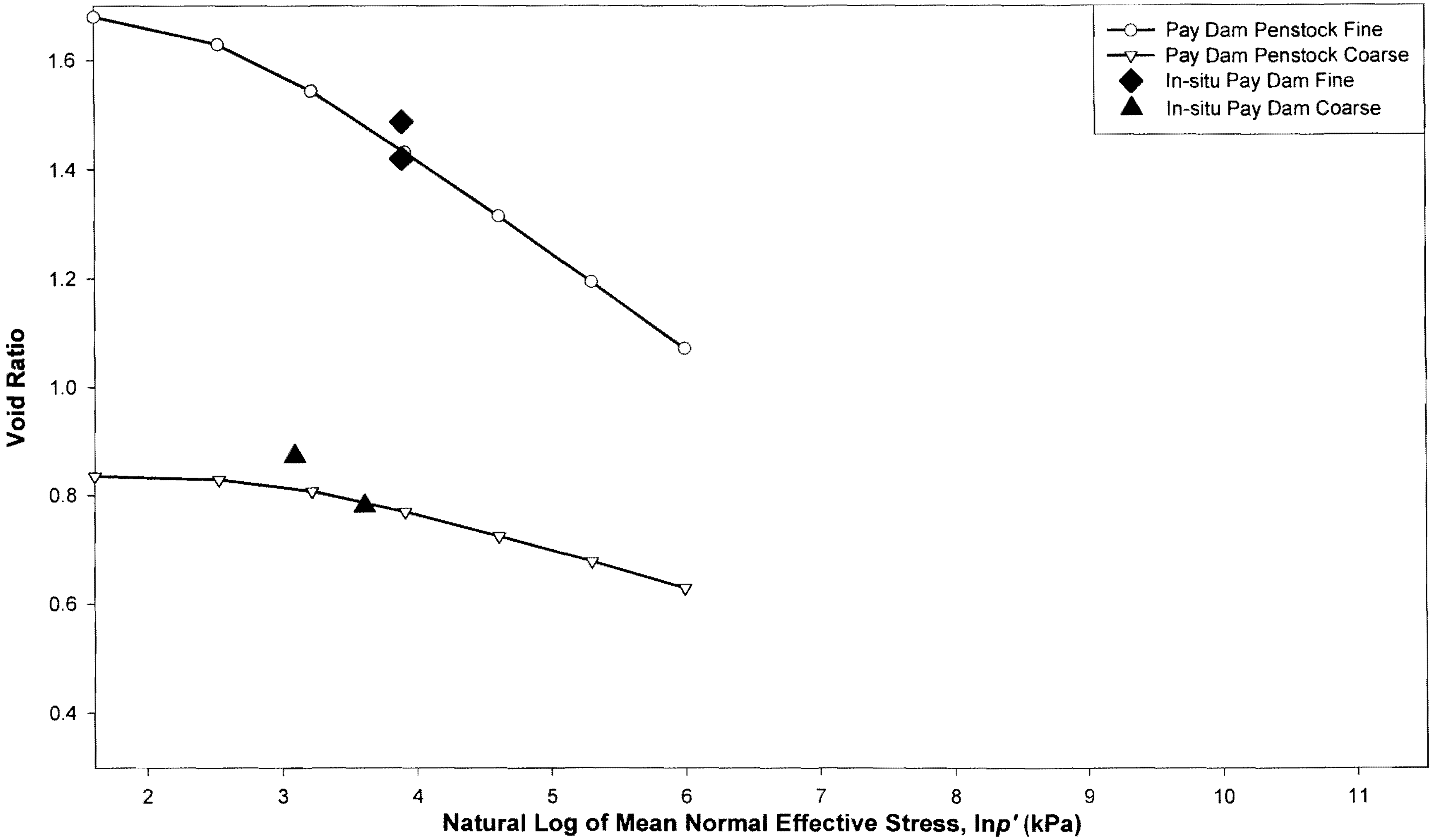


**Figure 4-13: In-situ undisturbed void ratio's compared with reconstituted compression curves.**

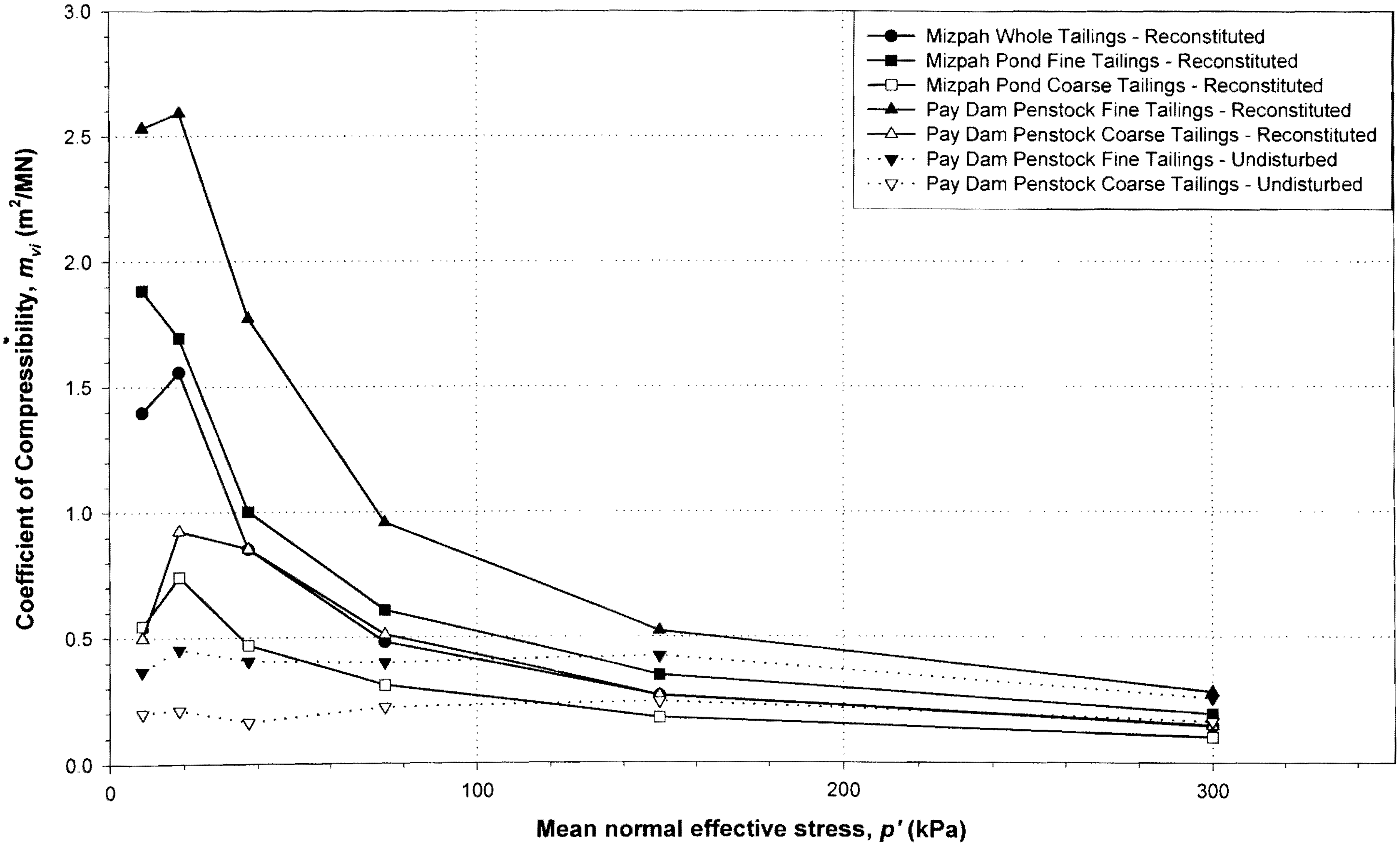


**Figure 4-14: Gold Tailings: Coefficient of Compressibility data.**

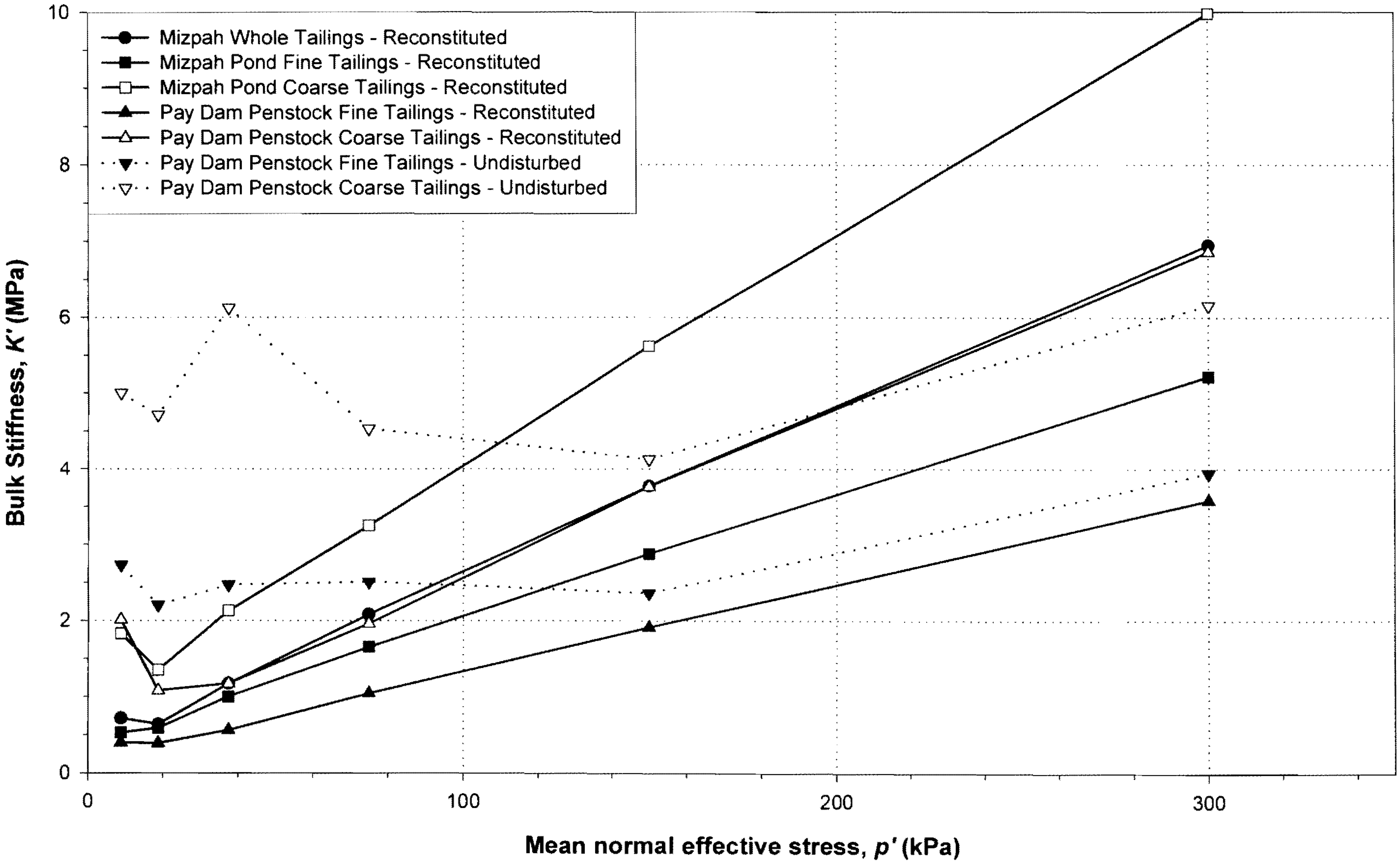


**Figure 4-15: Gold Tailings: Bulk Stiffness data.**

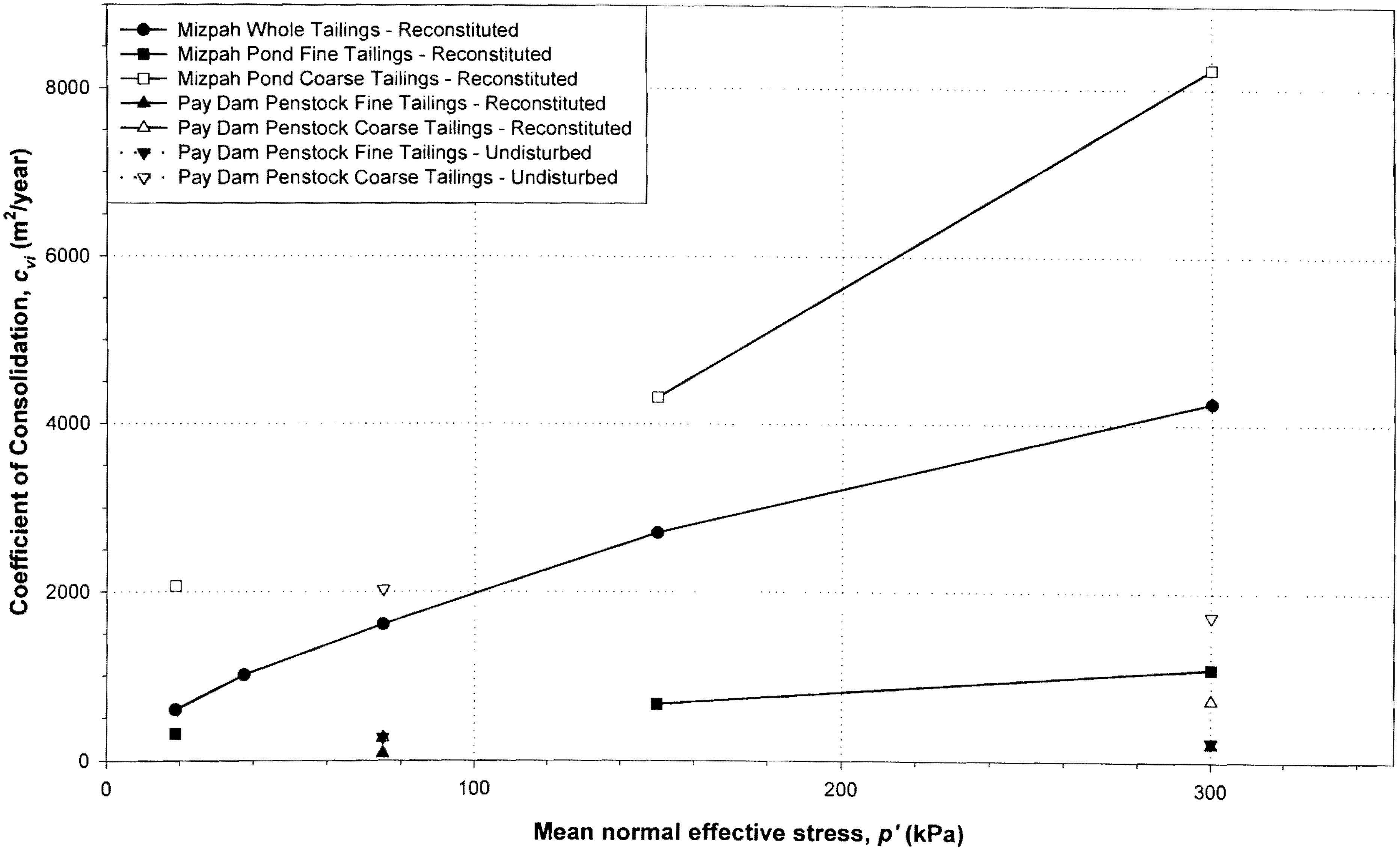


**Figure 4-16: Gold Tailings: Coefficient of Consolidation data.**

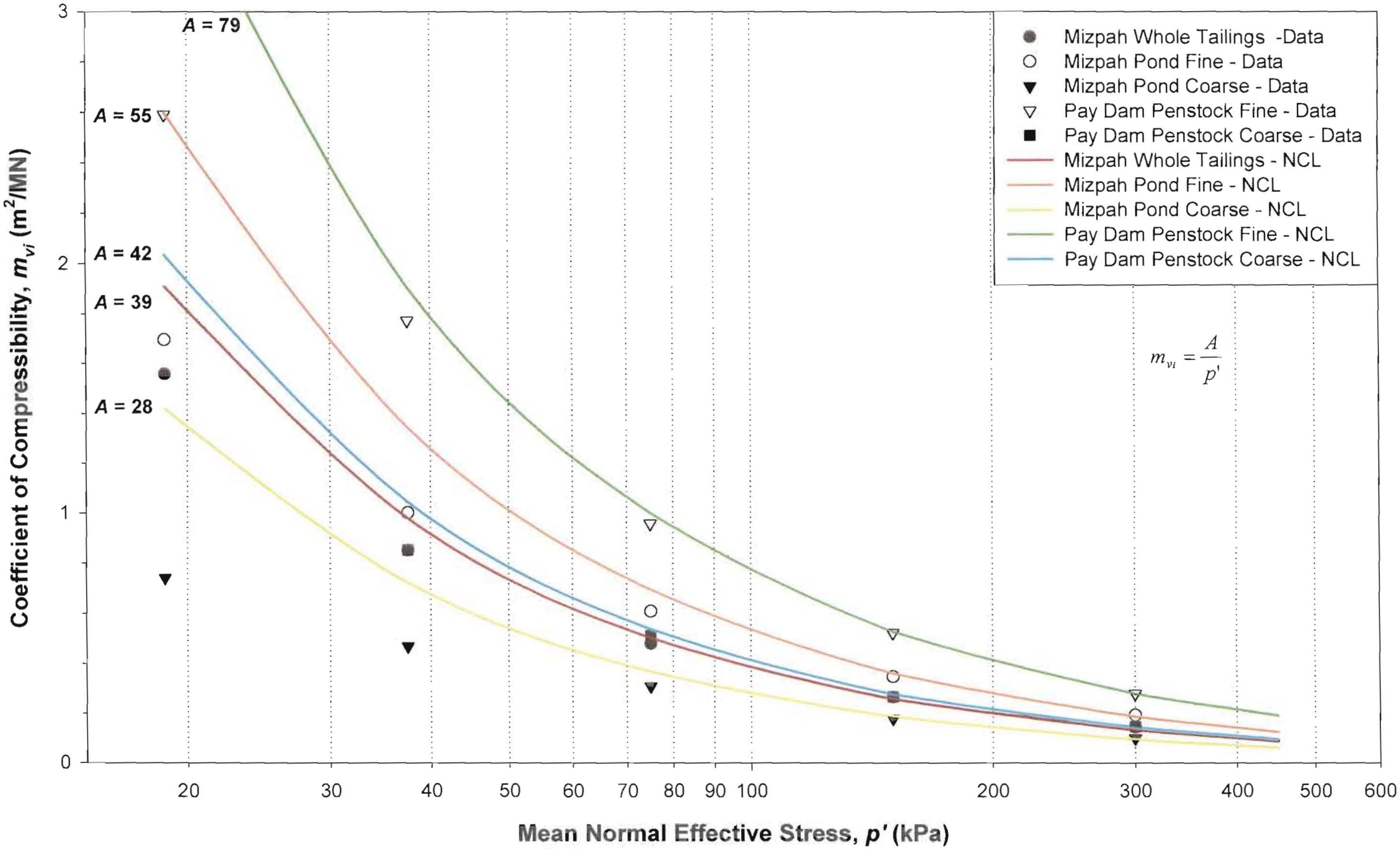


**Figure 4-17: Coefficient of Compressibility as a function of the isotropic confinement pressure.**

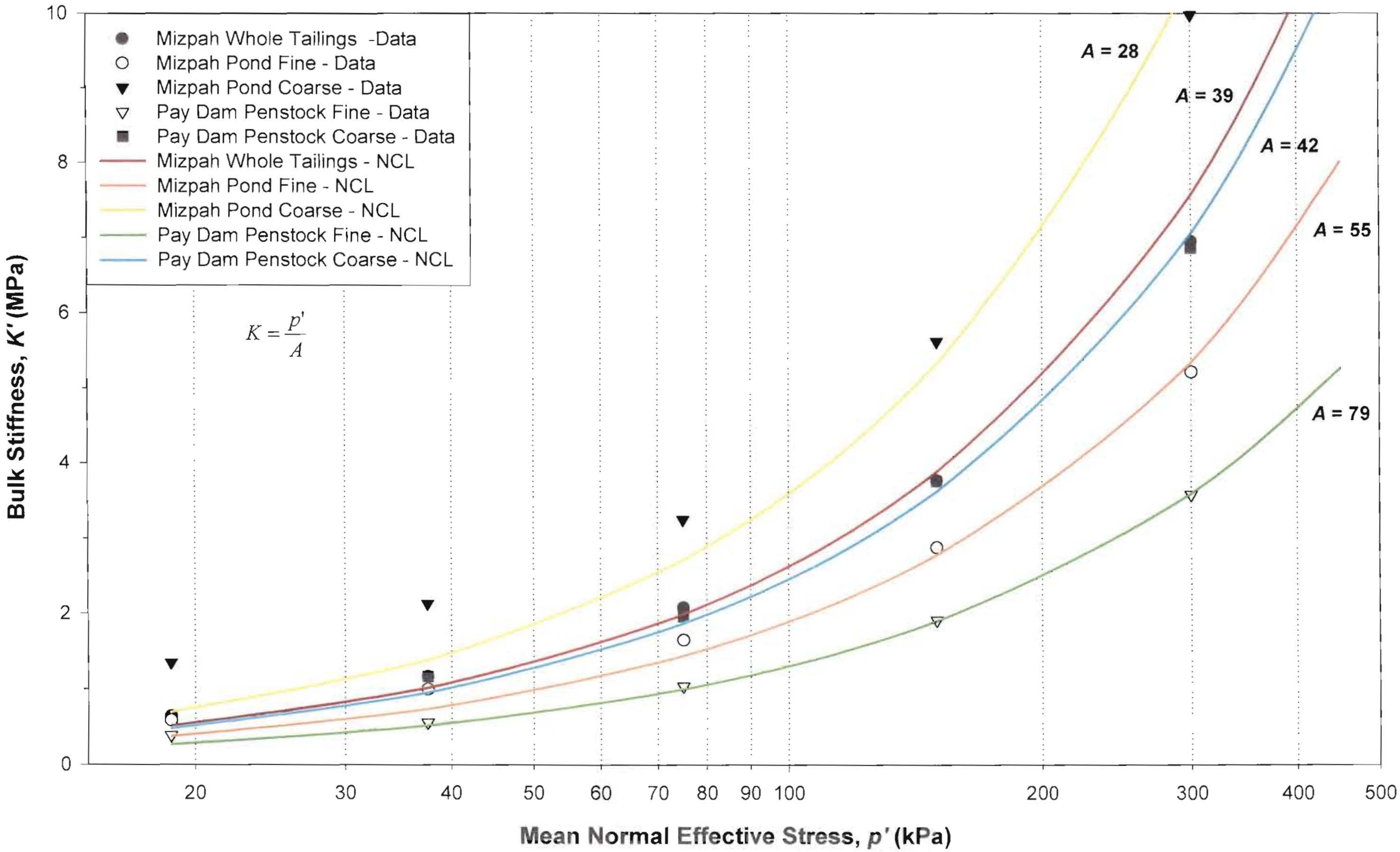


**Figure 4-18: Bulk Stiffness as a function of the isotropic confinement pressure.**

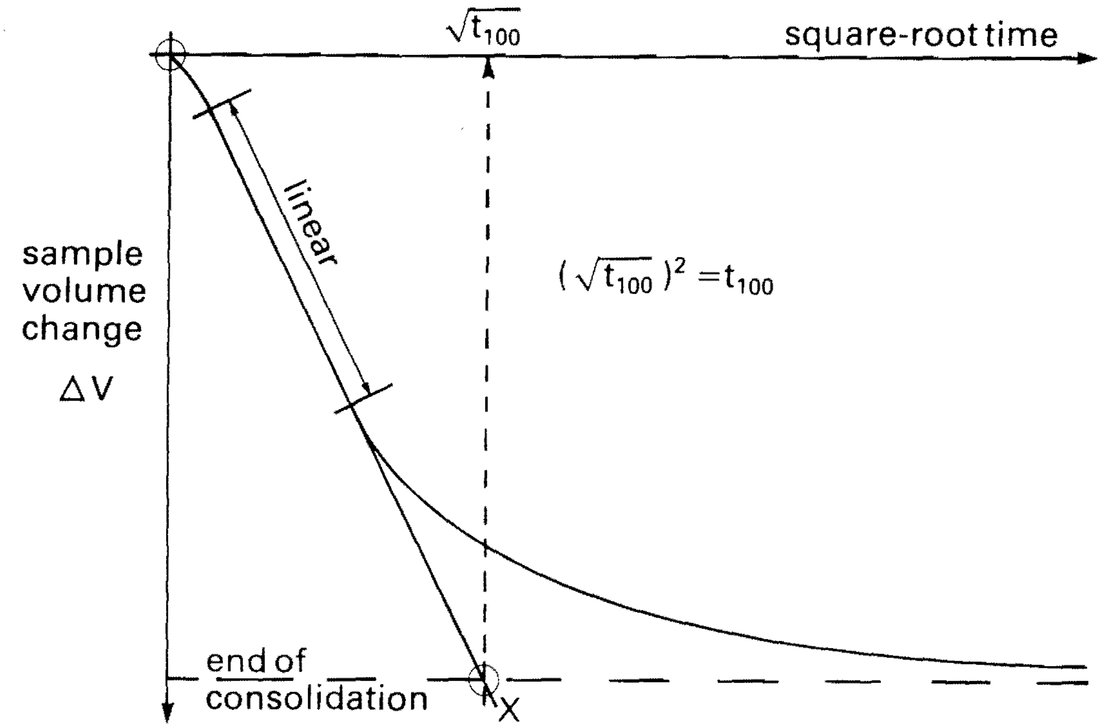


(a)

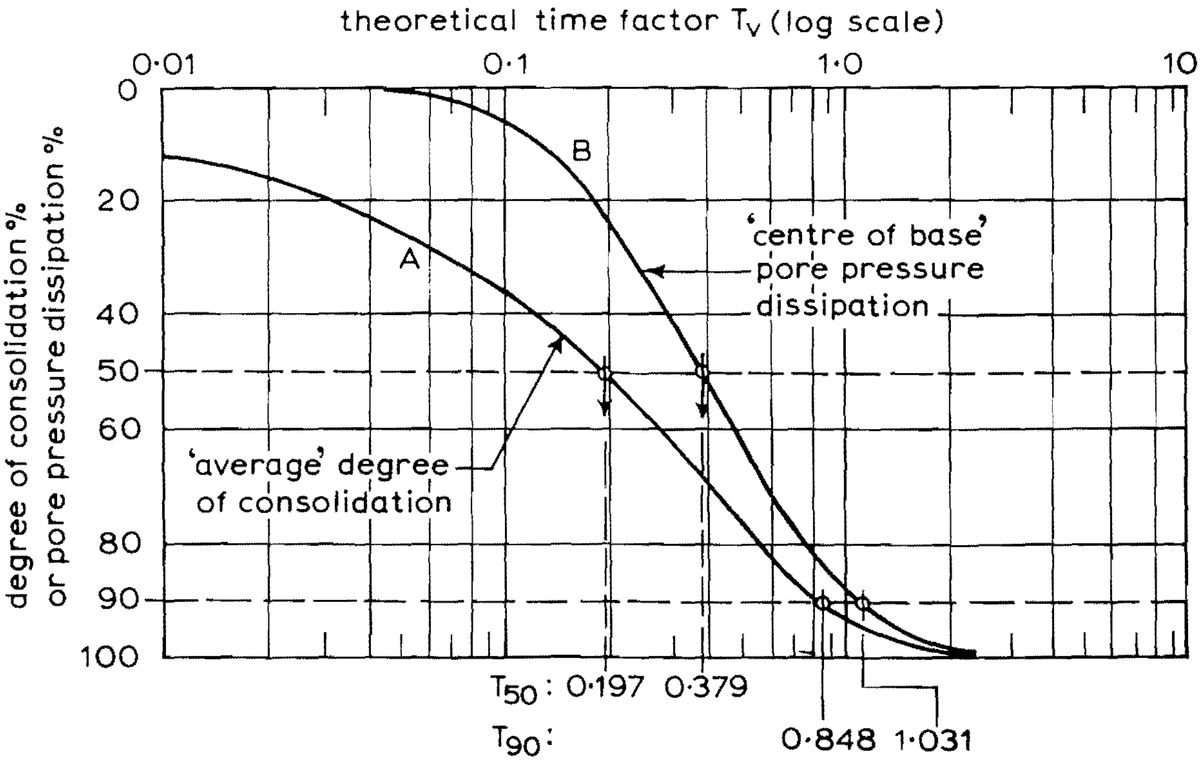


(b)

**Figure 4-19: (a) Derivation of theoretical $t_{100}$ from the volume change square root time consolidation curve for a triaxial specimen, (b) Theoretical relationships between time factor and degree of consolidation for vertical triaxial drainage for two methods of measurement.**

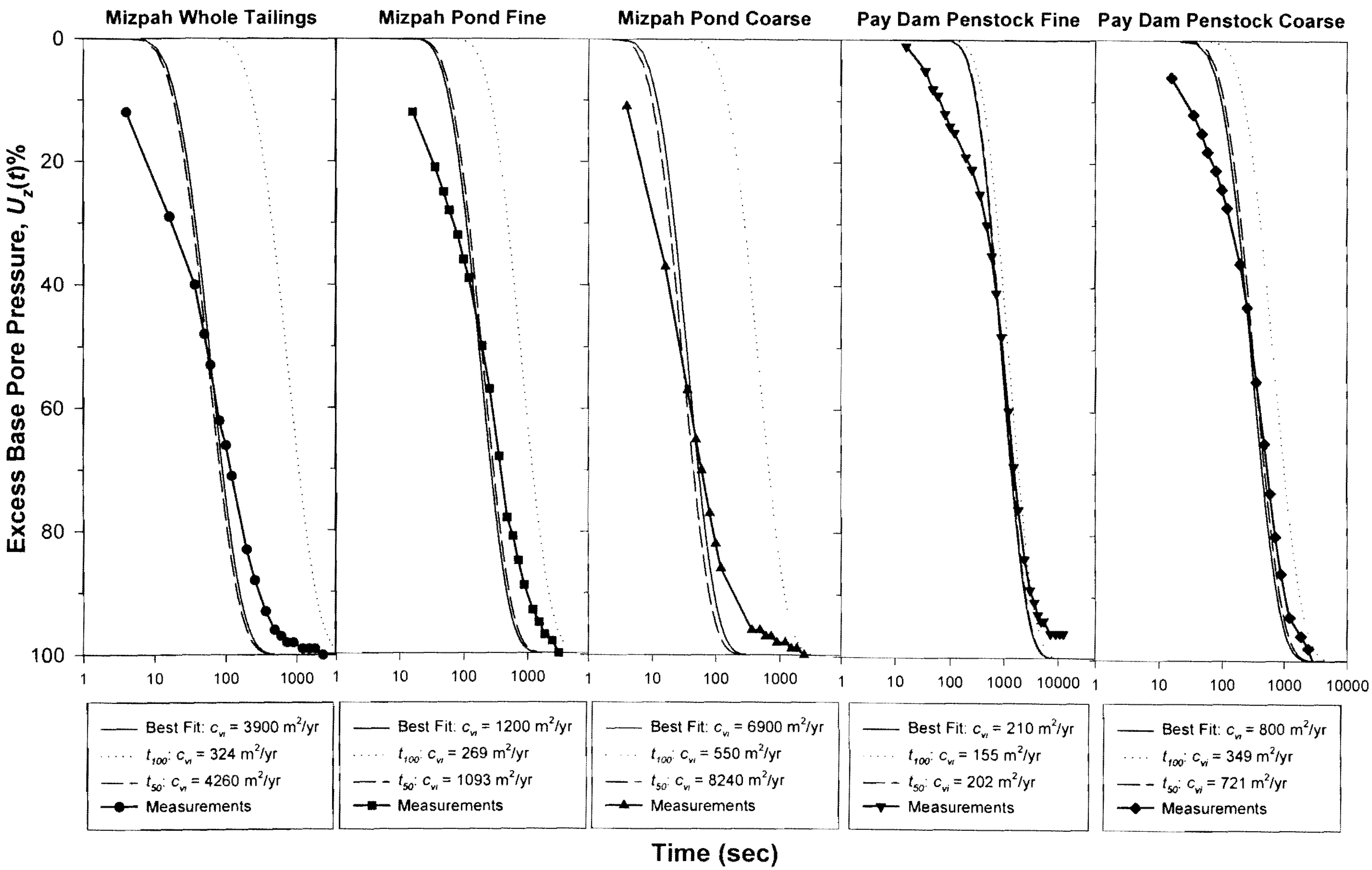


**Figure 4-20: Pore pressure dissipation data compared with theoretical curves.**

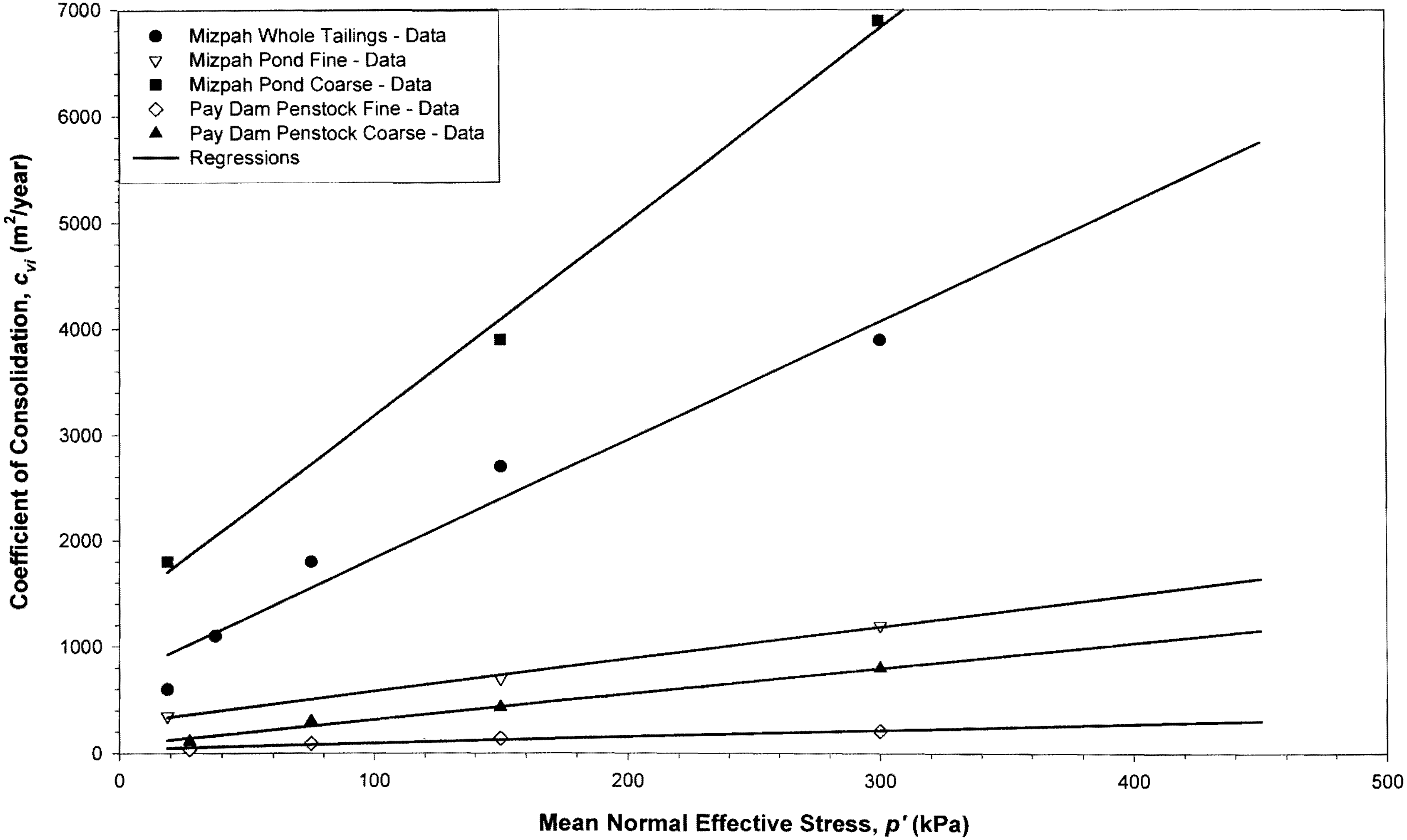


**Figure 4-21: Coefficient of Consolidation as a function of the isotropic confinement pressure.**

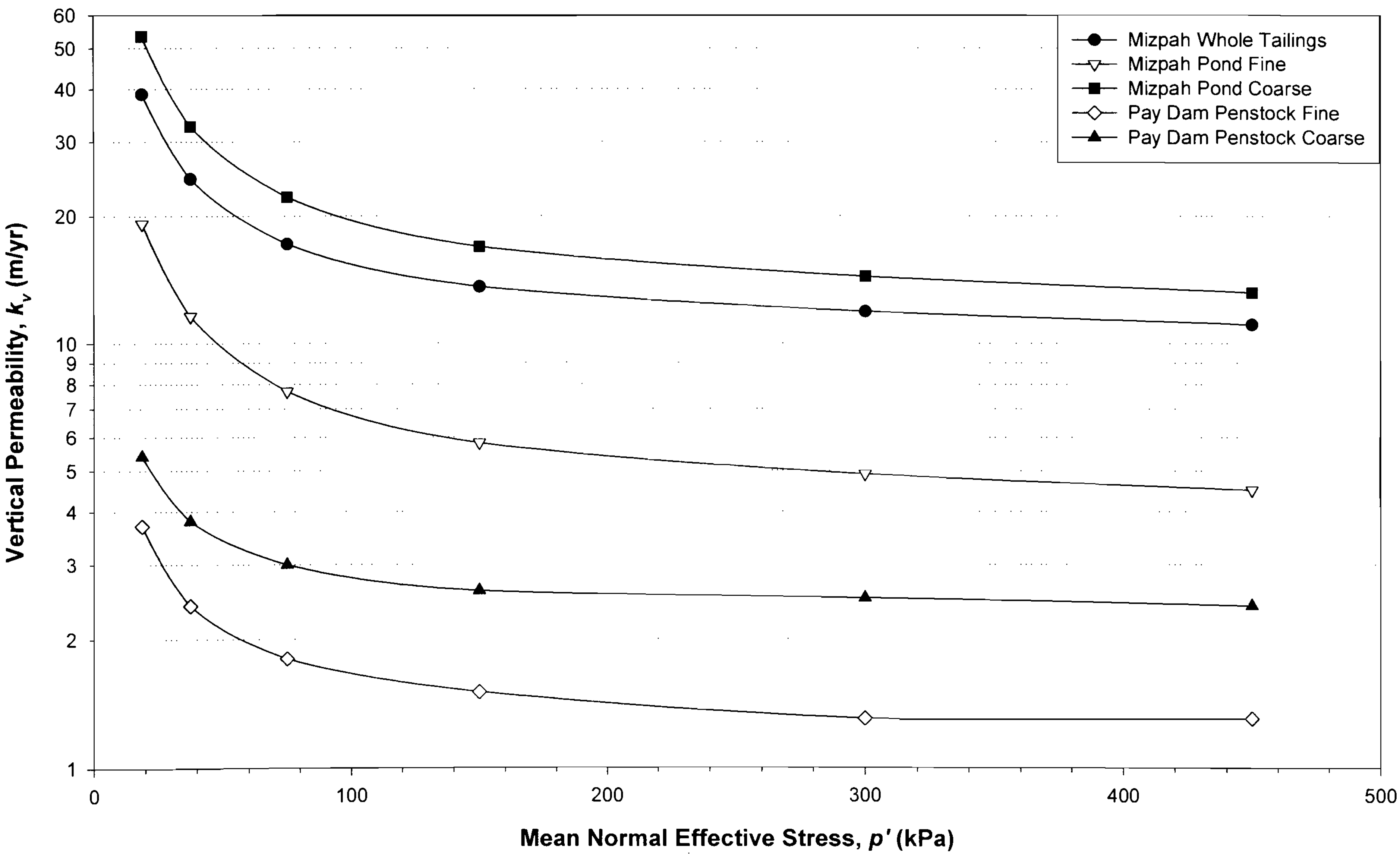


**Figure 4-22: Vertical permeability as a function of the confinement pressure.**

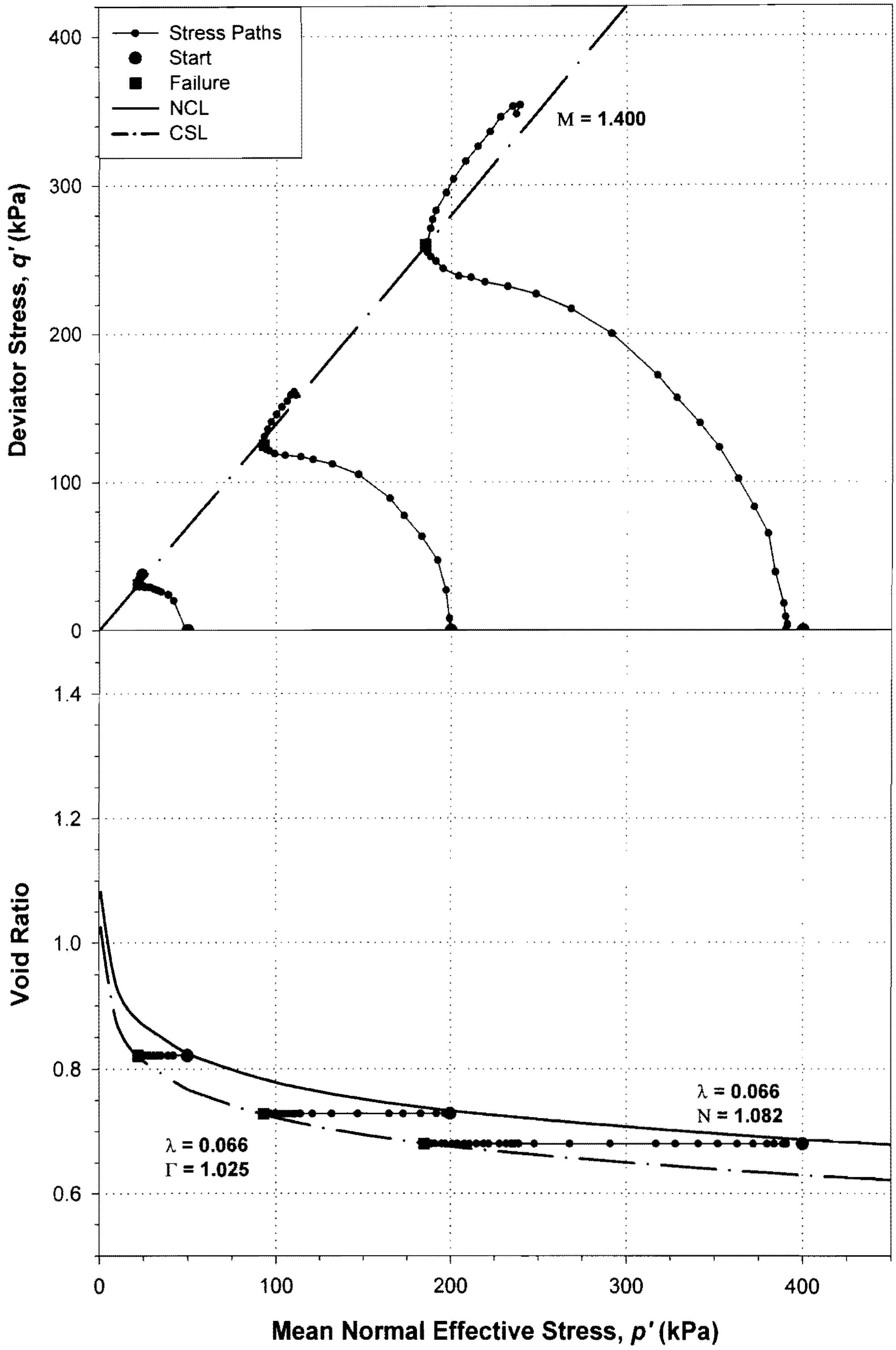


**Figure 4-23: Critical state parameters for reconstituted Mizpah whole tailings.**

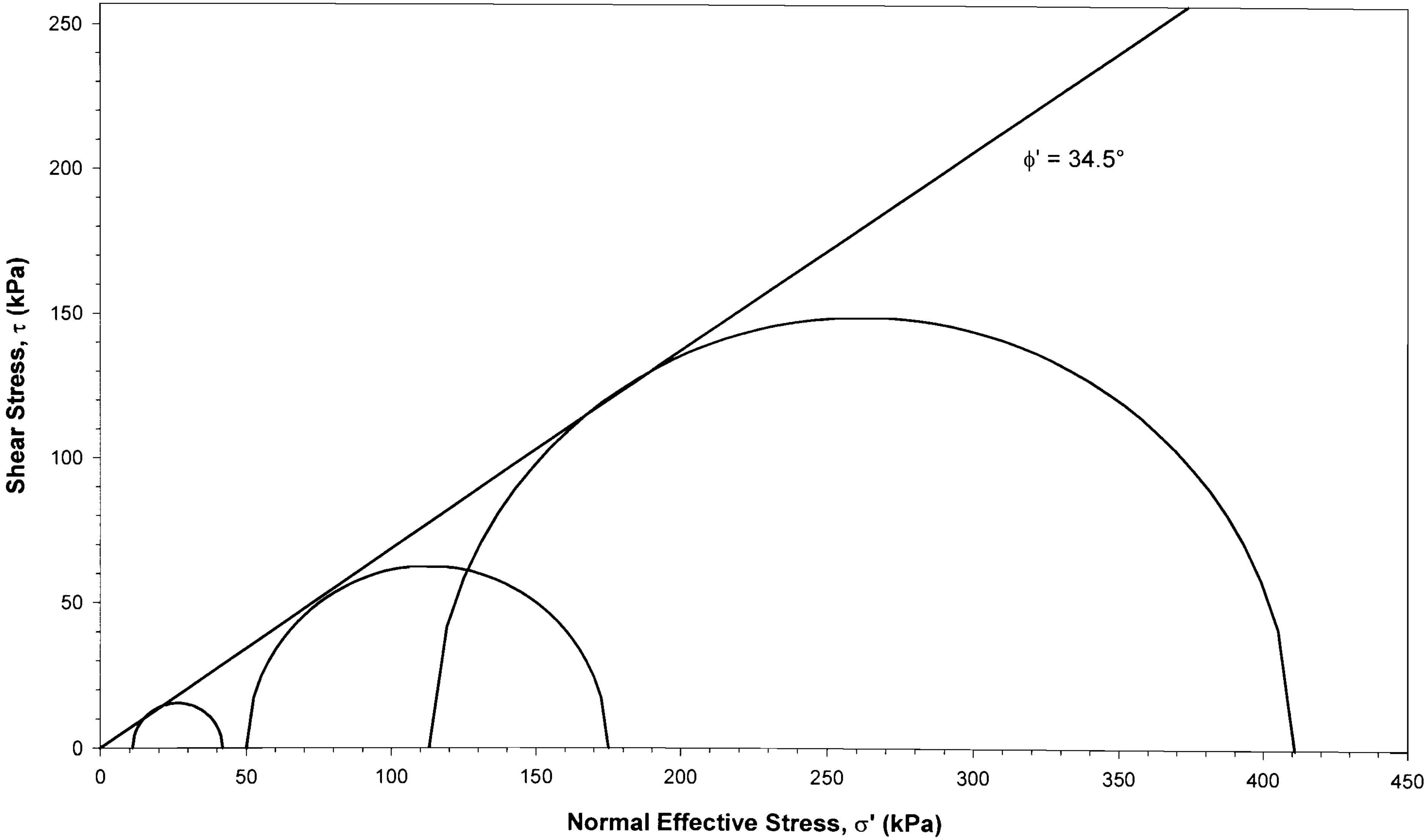


Figure 4-24: Mohr's Circles for reconstituted Mizpah whole tailings.

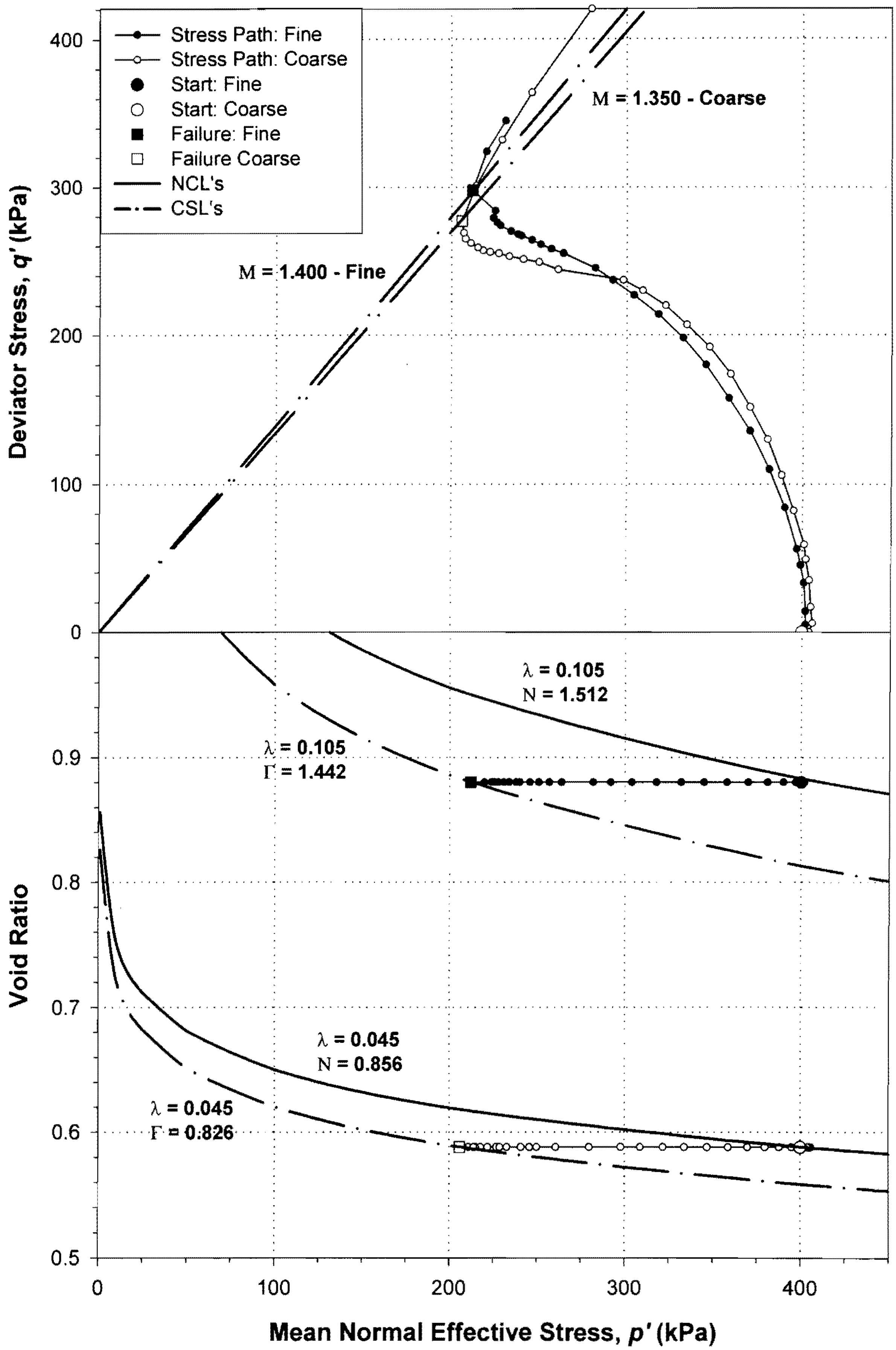


**Figure 4-25: Critical state parameters for reconstituted Mizpah pond tailings.**

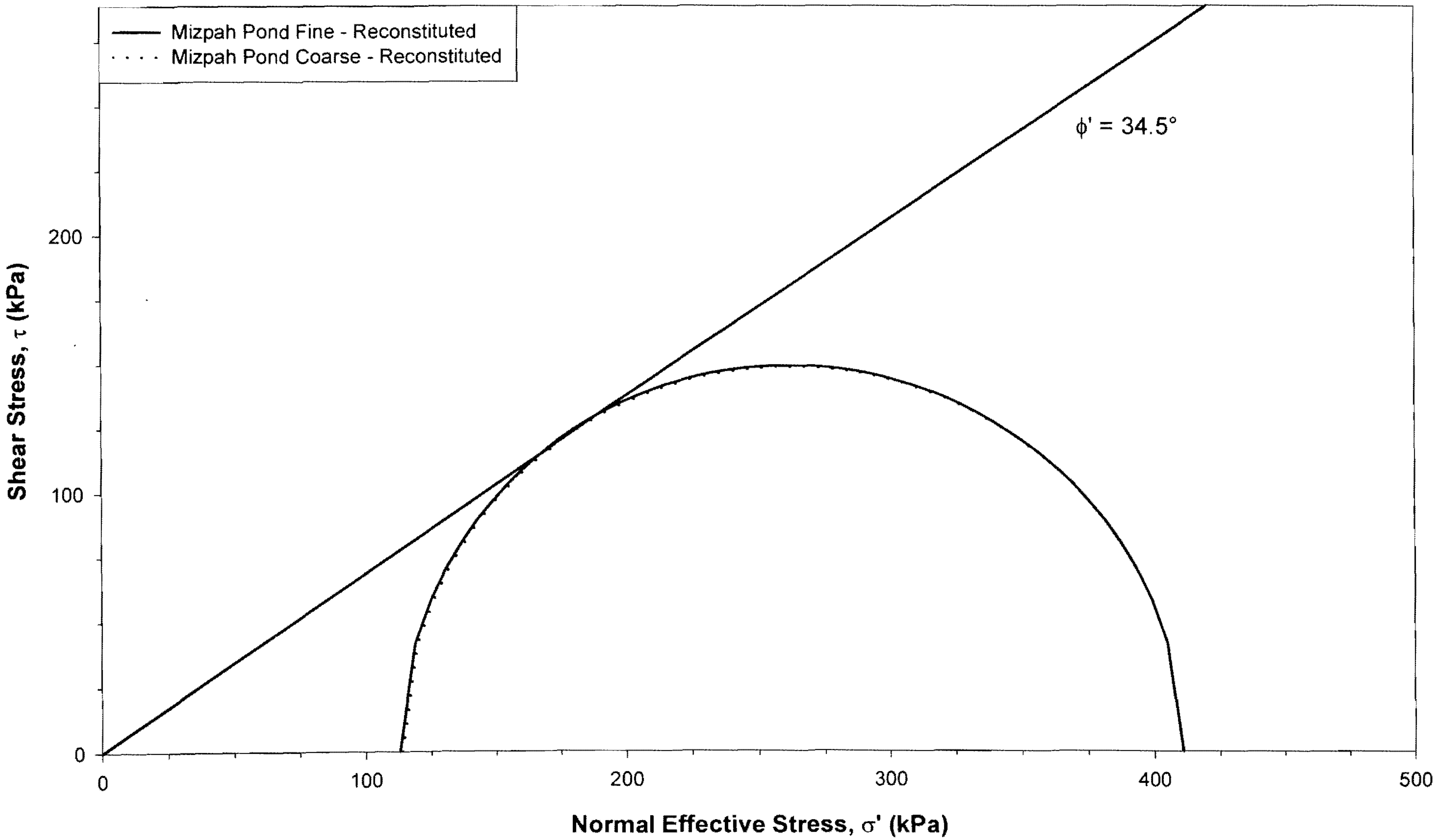


**Figure 4-26: Mohr's Circles for reconstituted Mizpah pond tailings.**

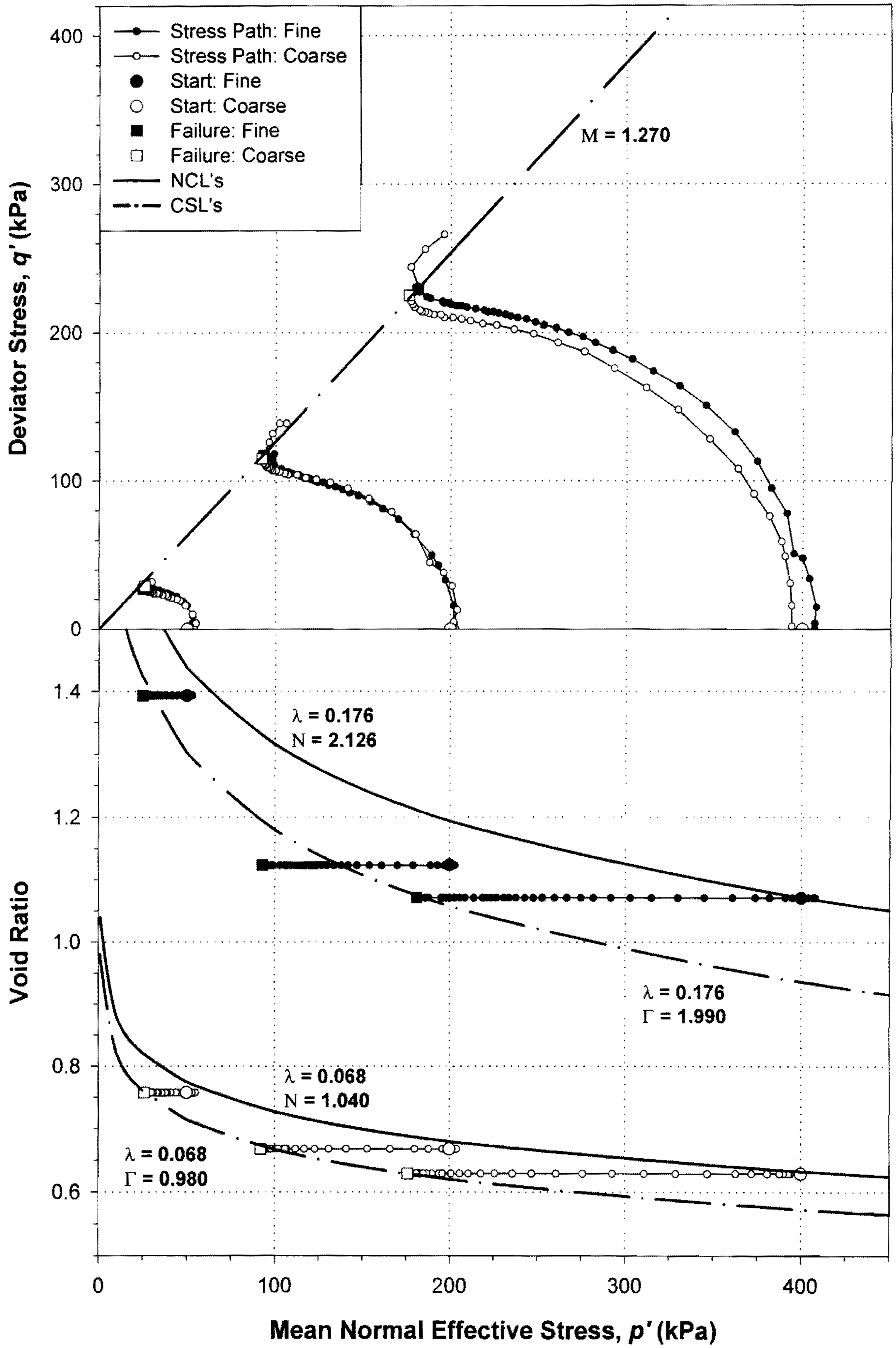


**Figure 4-27: Critical state parameters for reconstituted Pay Dam penstock tailings.**

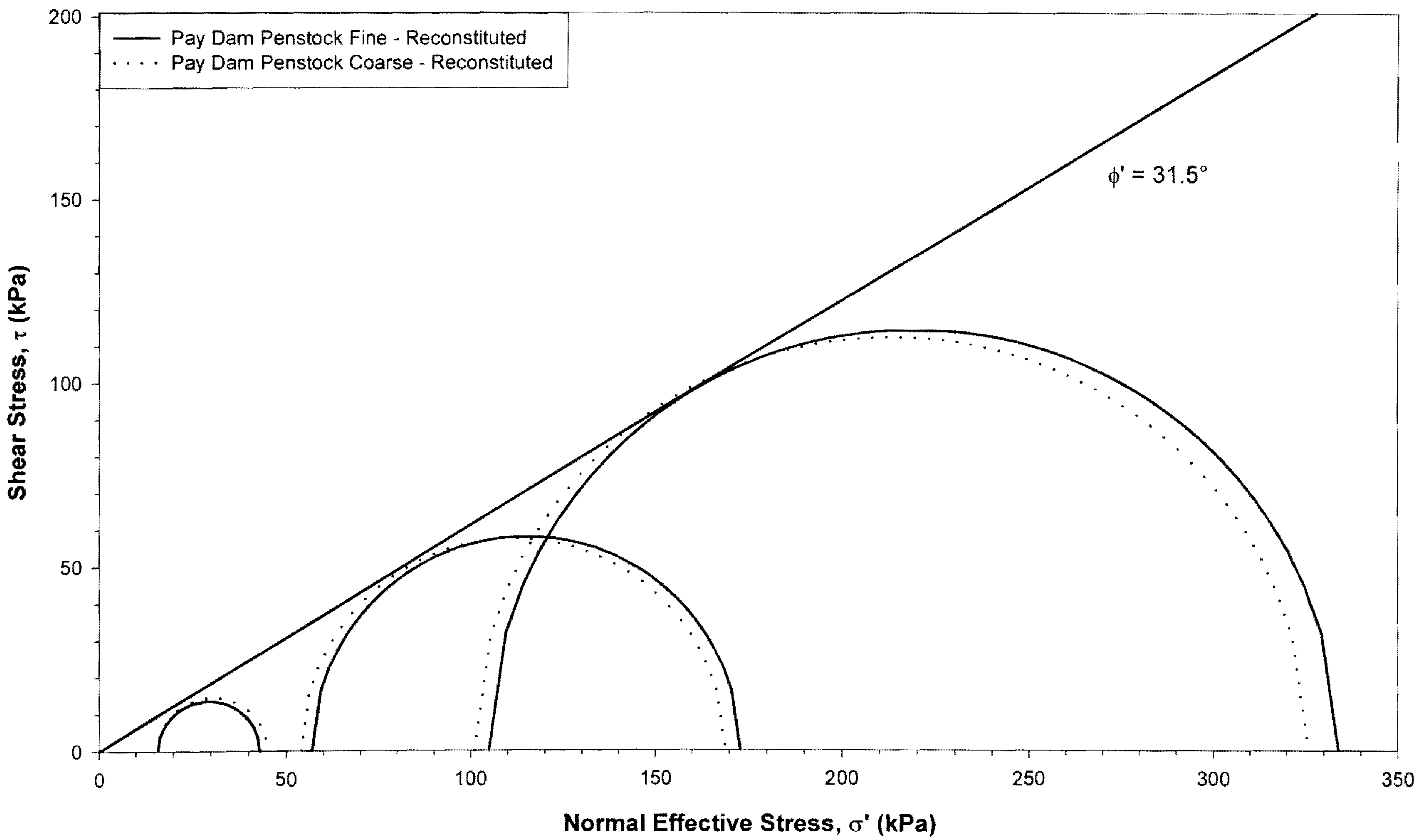


**Figure 4-28: Mohr's Circles for reconstituted Pay Dam penstock tailings.**

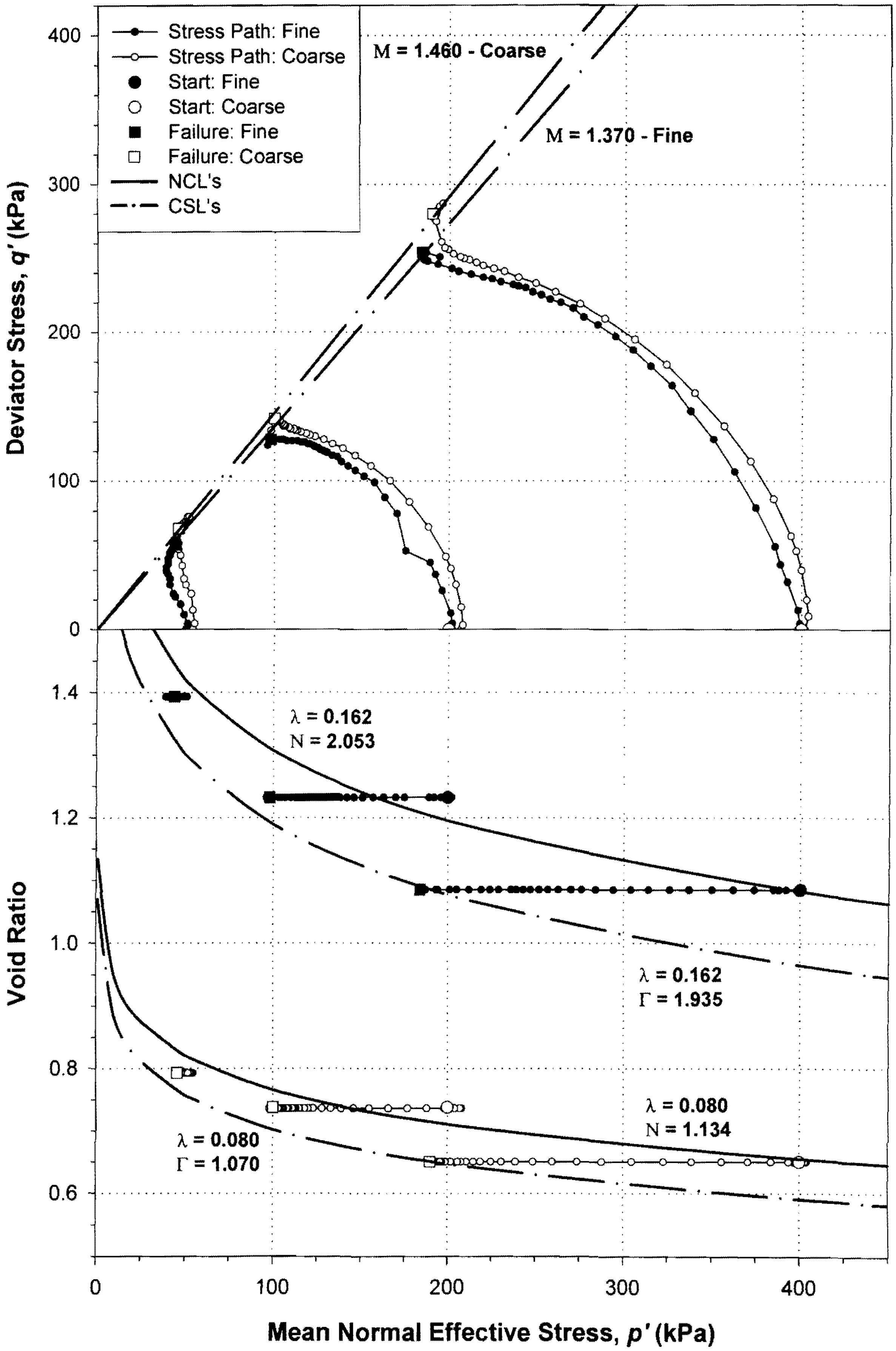


Figure 4-29: Critical state parameters for undisturbed Pay Dam penstock tailings.

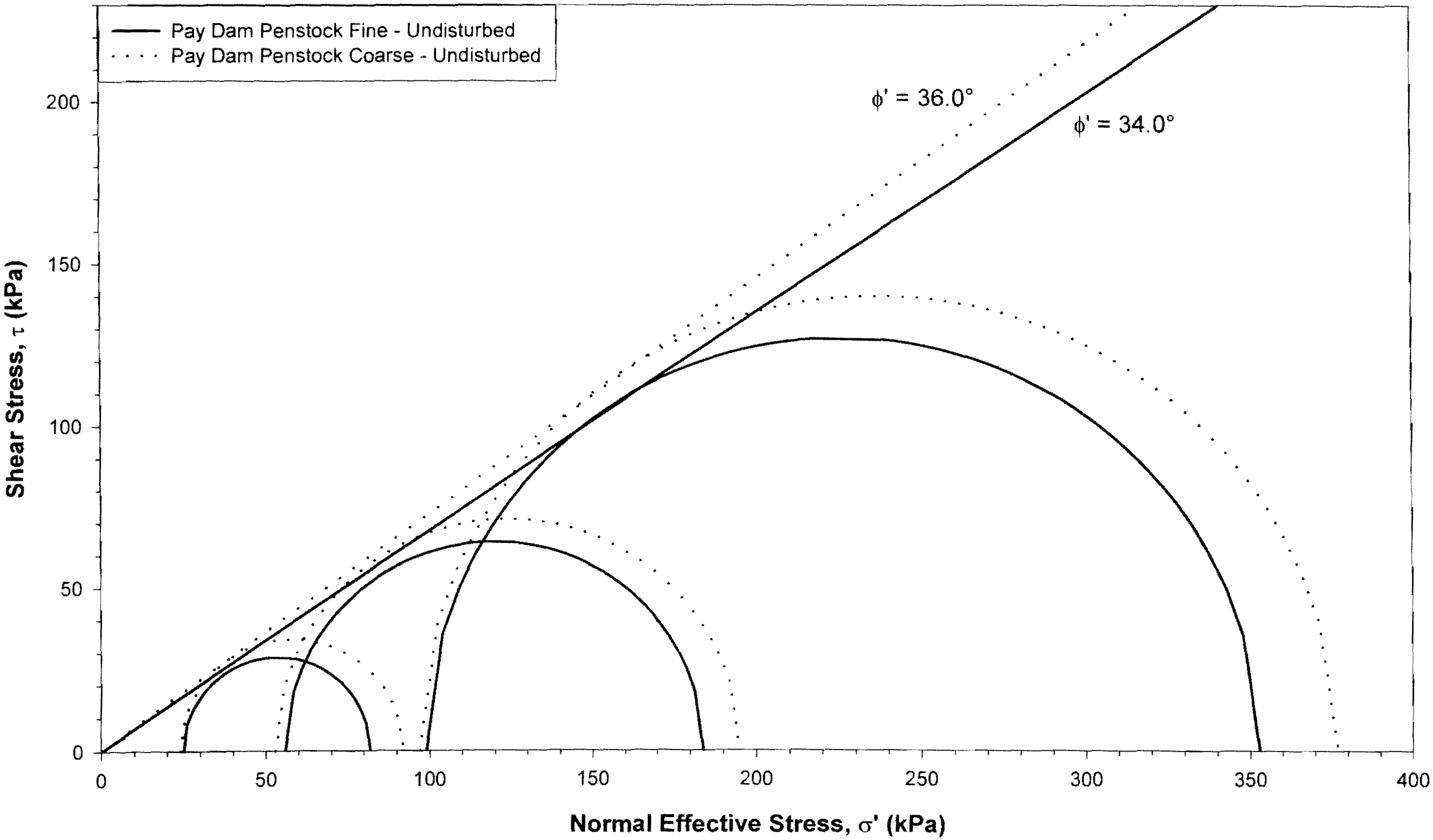


**Figure 4-30: Mohr's Circles for undisturbed Pay Dam penstock tailings.**

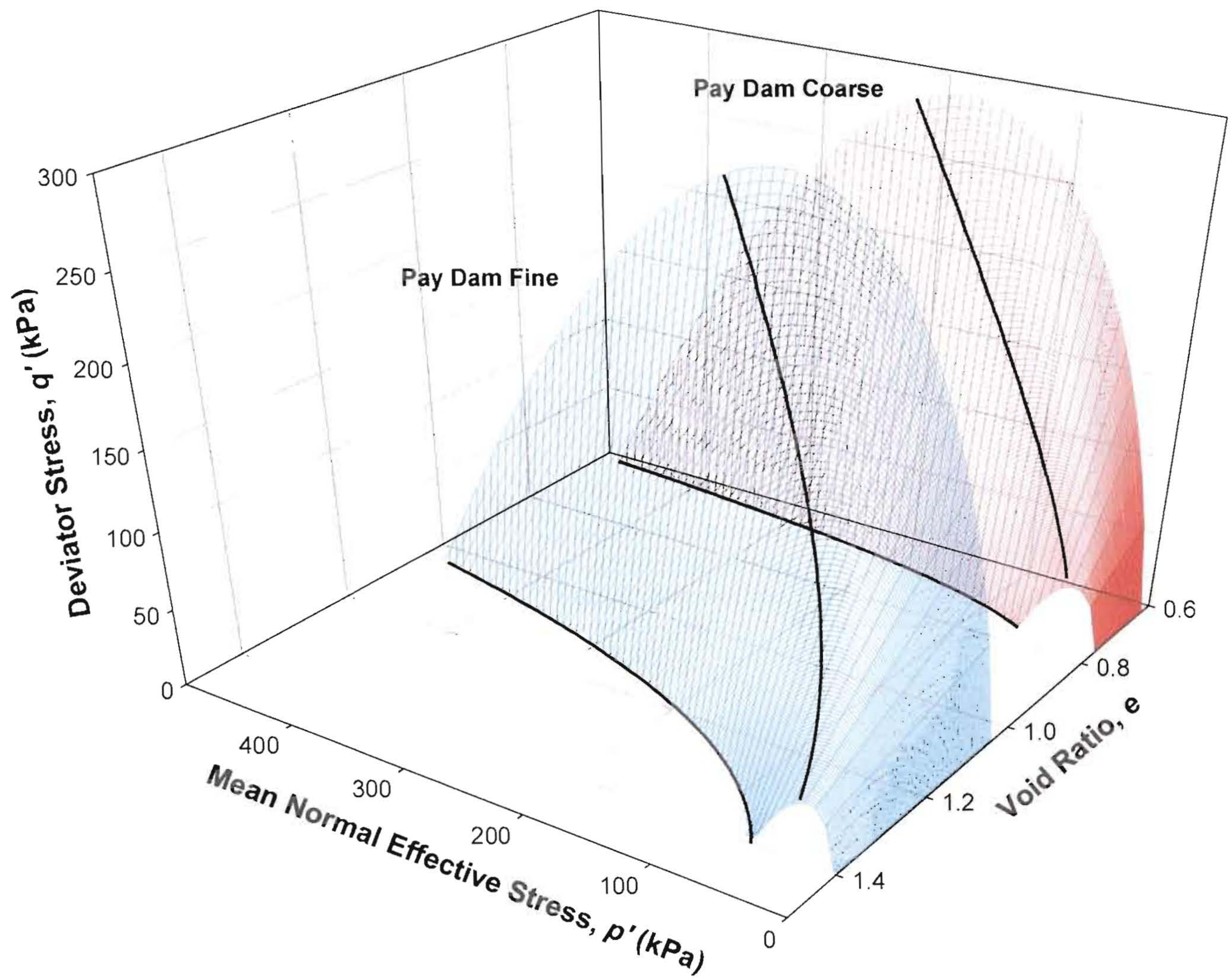


**Figure 4-31: Isometric view of the Cam-Clay state boundary surfaces for Pay Dam penstock tailings.**

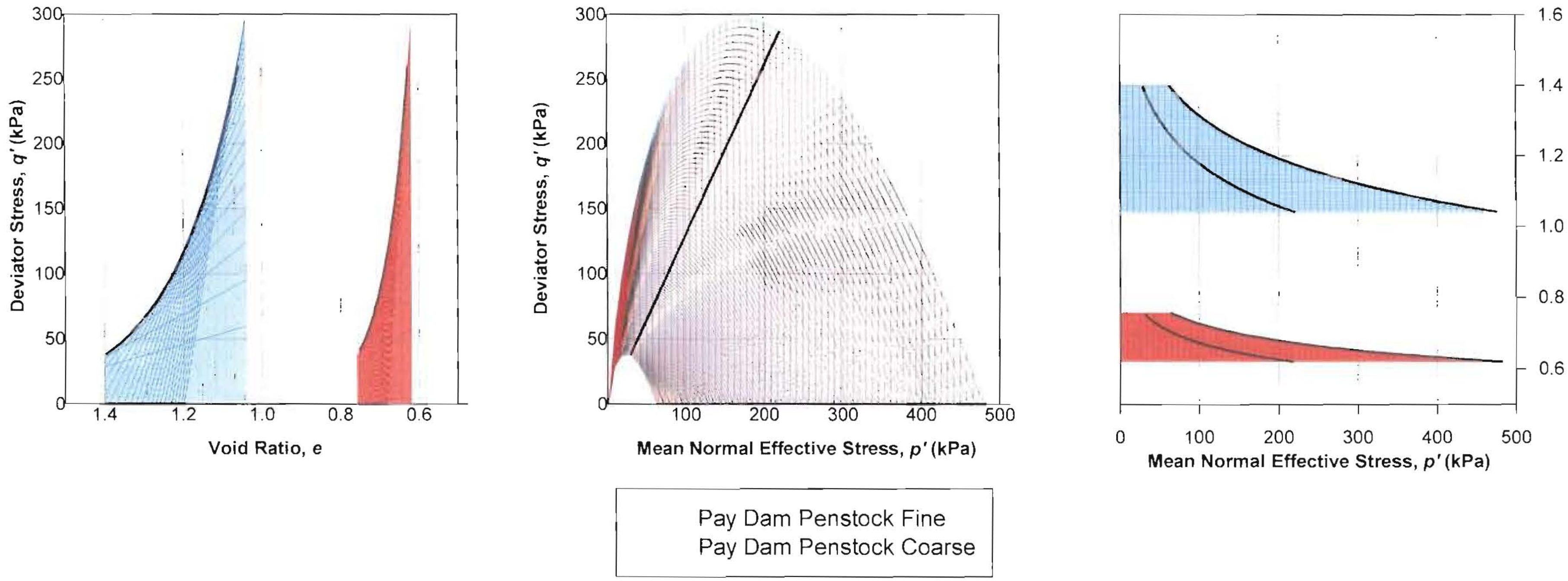


Figure 4-32: Two dimensional projections of the Pay Dam Cam-Clay state boundary surfaces.

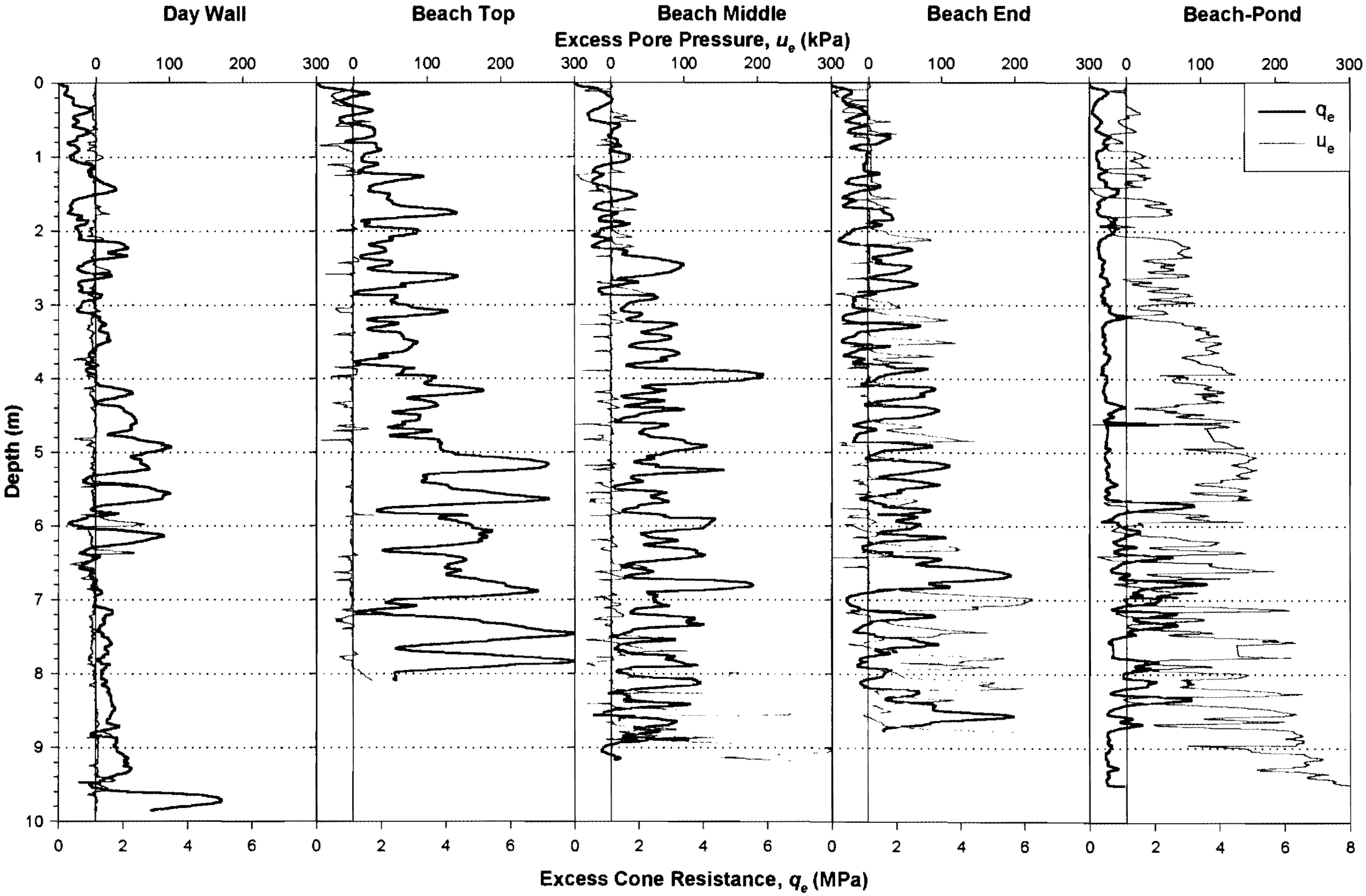


**Figure 4-33: Piezocone probe results for a cross section of the Mizpah tailings dam.**

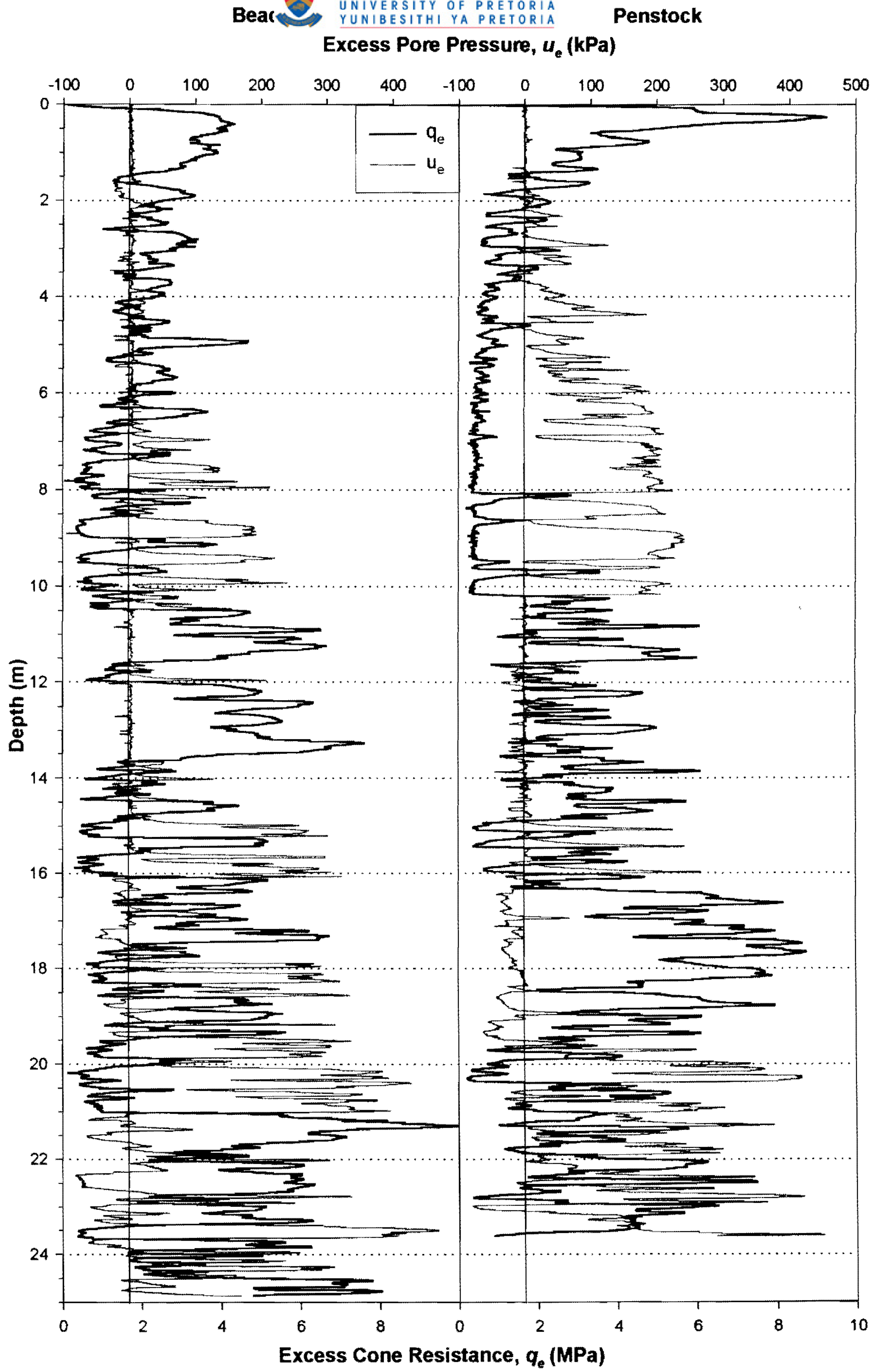


Figure 4-34: Piezocone probe results on Pay Dam for the Beach and Penstock locations.

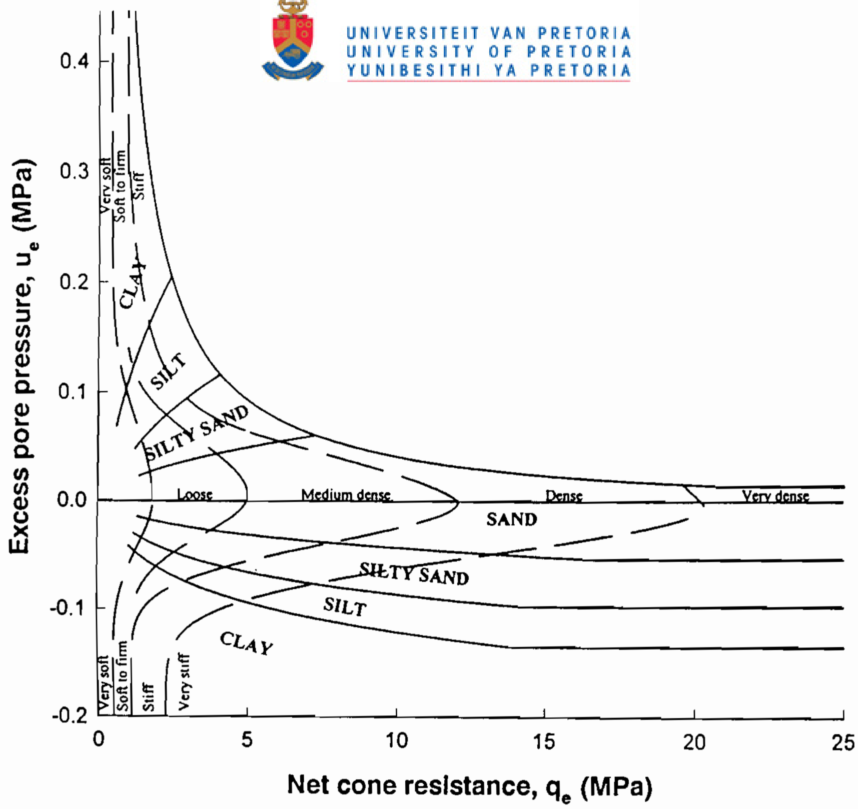


(a)

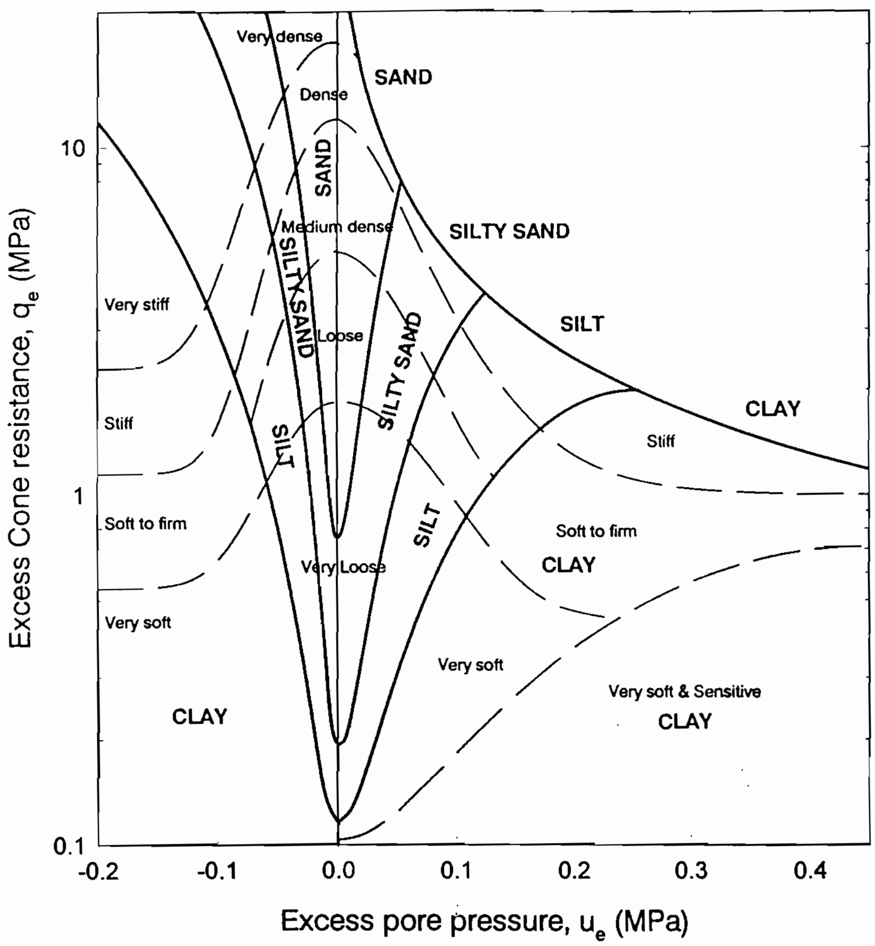


(b)

**Figure 4-35: (a) The Jones and Rust (1982) soils identification chart for use with the piezocone, (b) as modified by the author.**

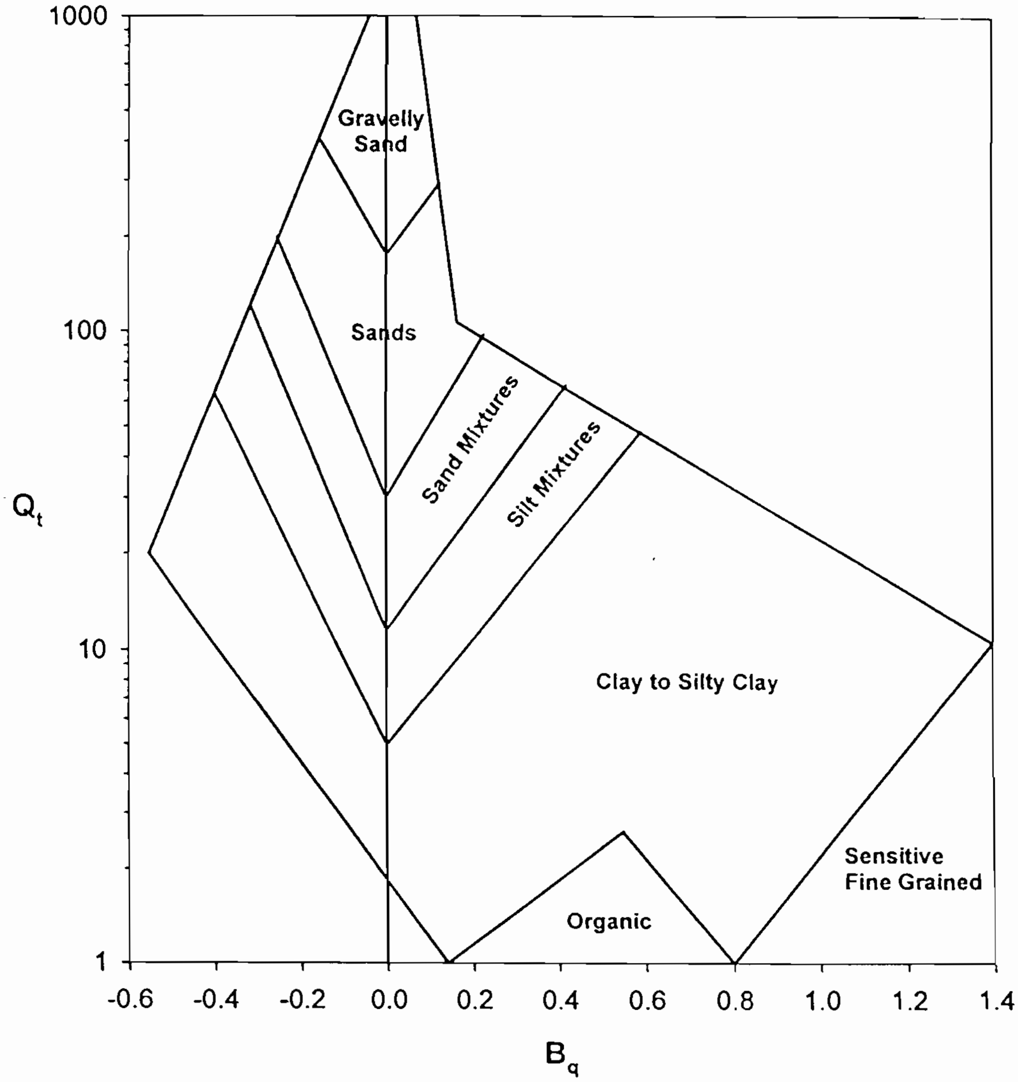


**Figure 4-36: The Robertson and Campanella soils identification charts for use with the piezocone (Robertson, 1990).**

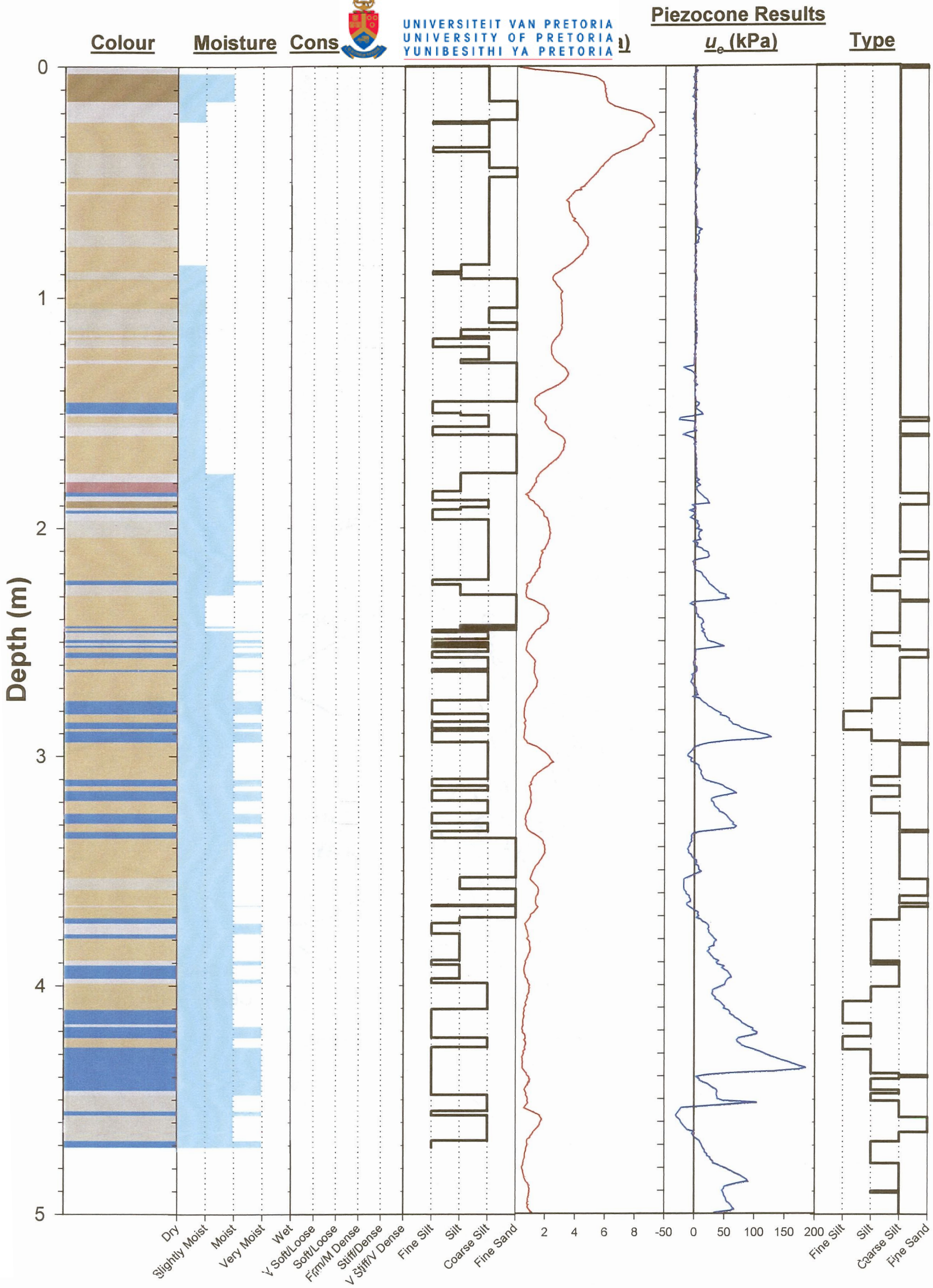


**Figure 4-37: Piezocone penetration data compared with the in-situ profile for Pay Dam Penstock.**

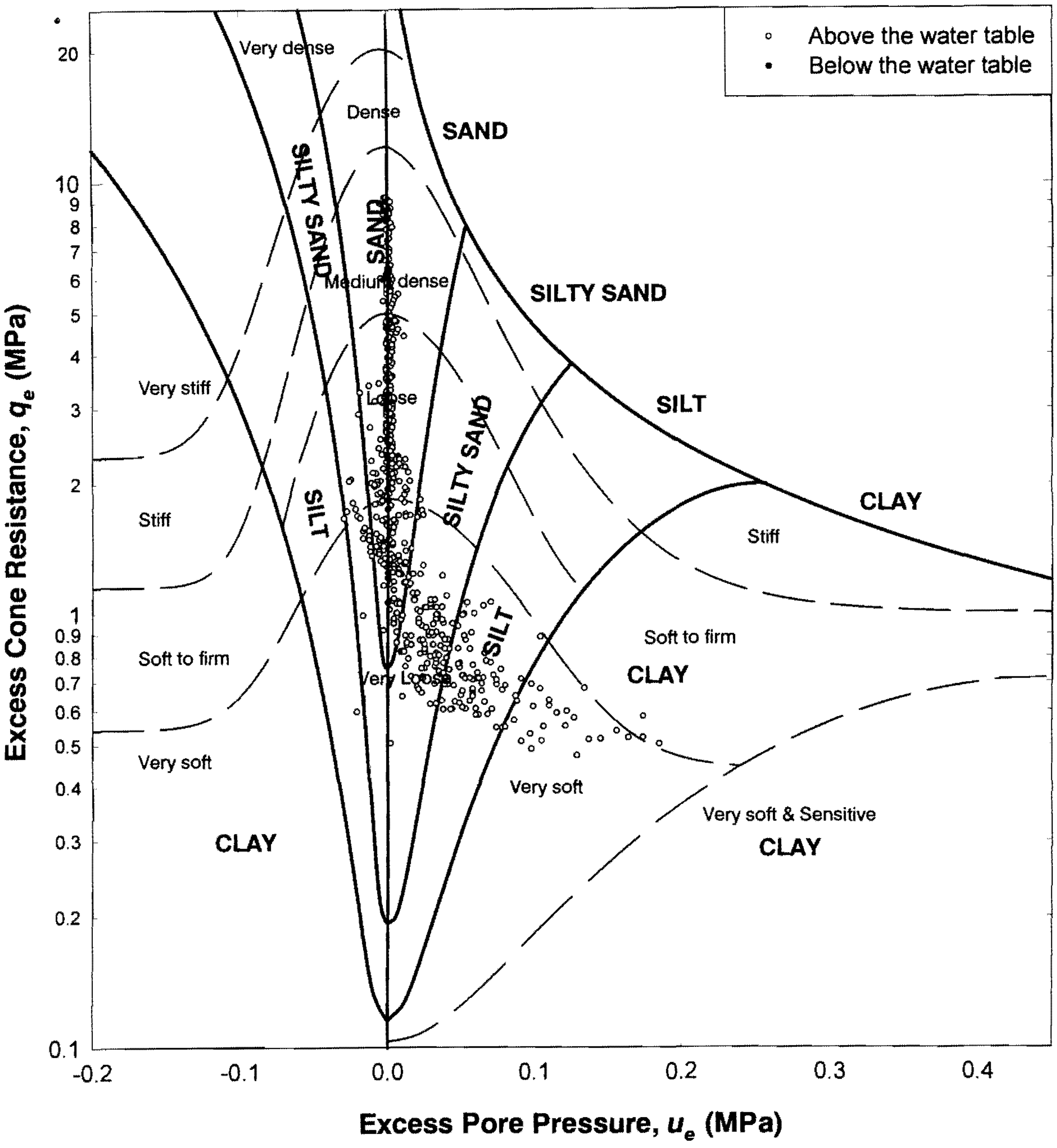


**Figure 4-38: Penetration data for Pay Dam Penstock represented on the soils identification chart.**

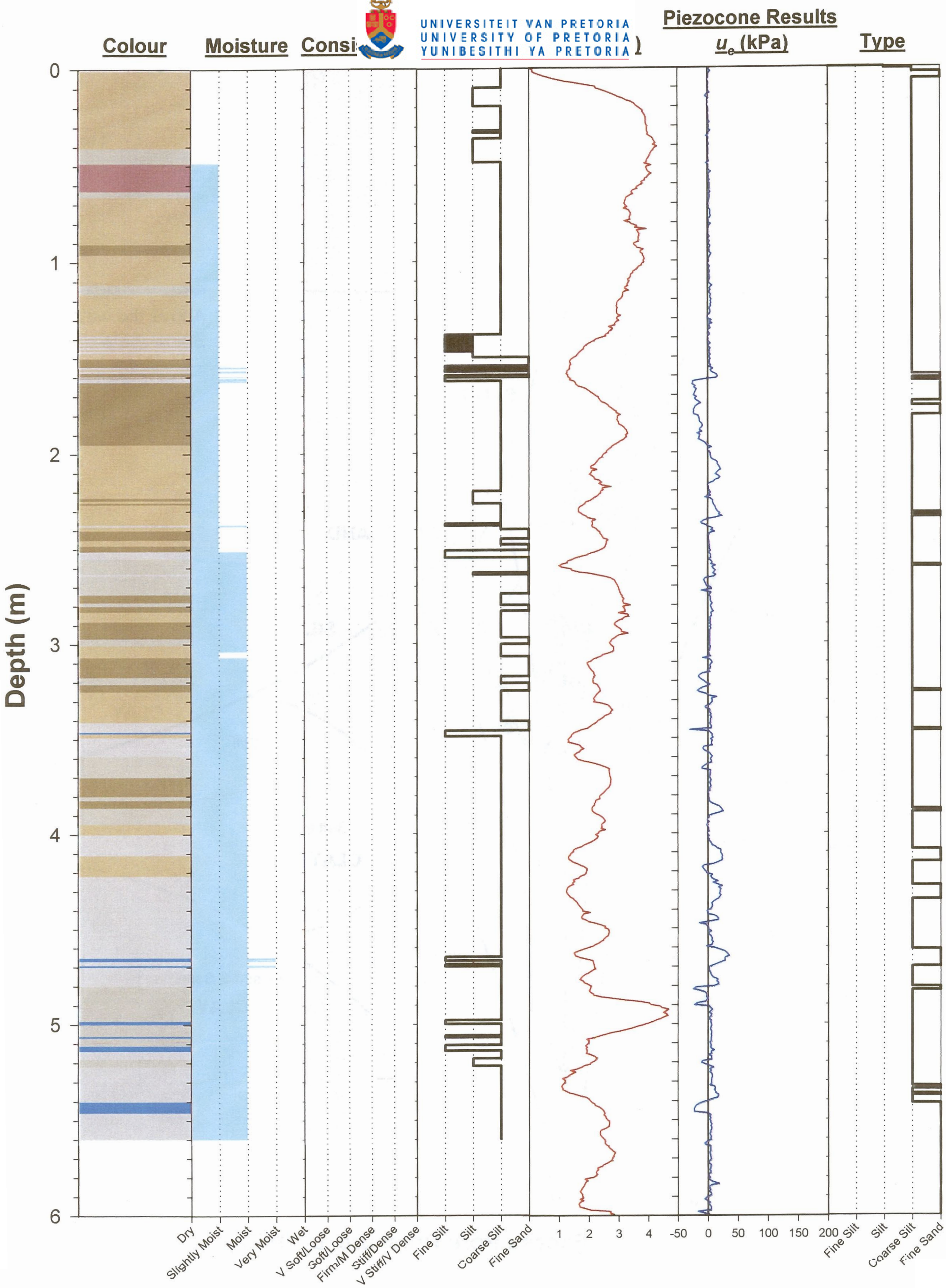


**Figure 4-39: Piezocone penetration data compared with the in-situ profile for Pay Dam Beach.**

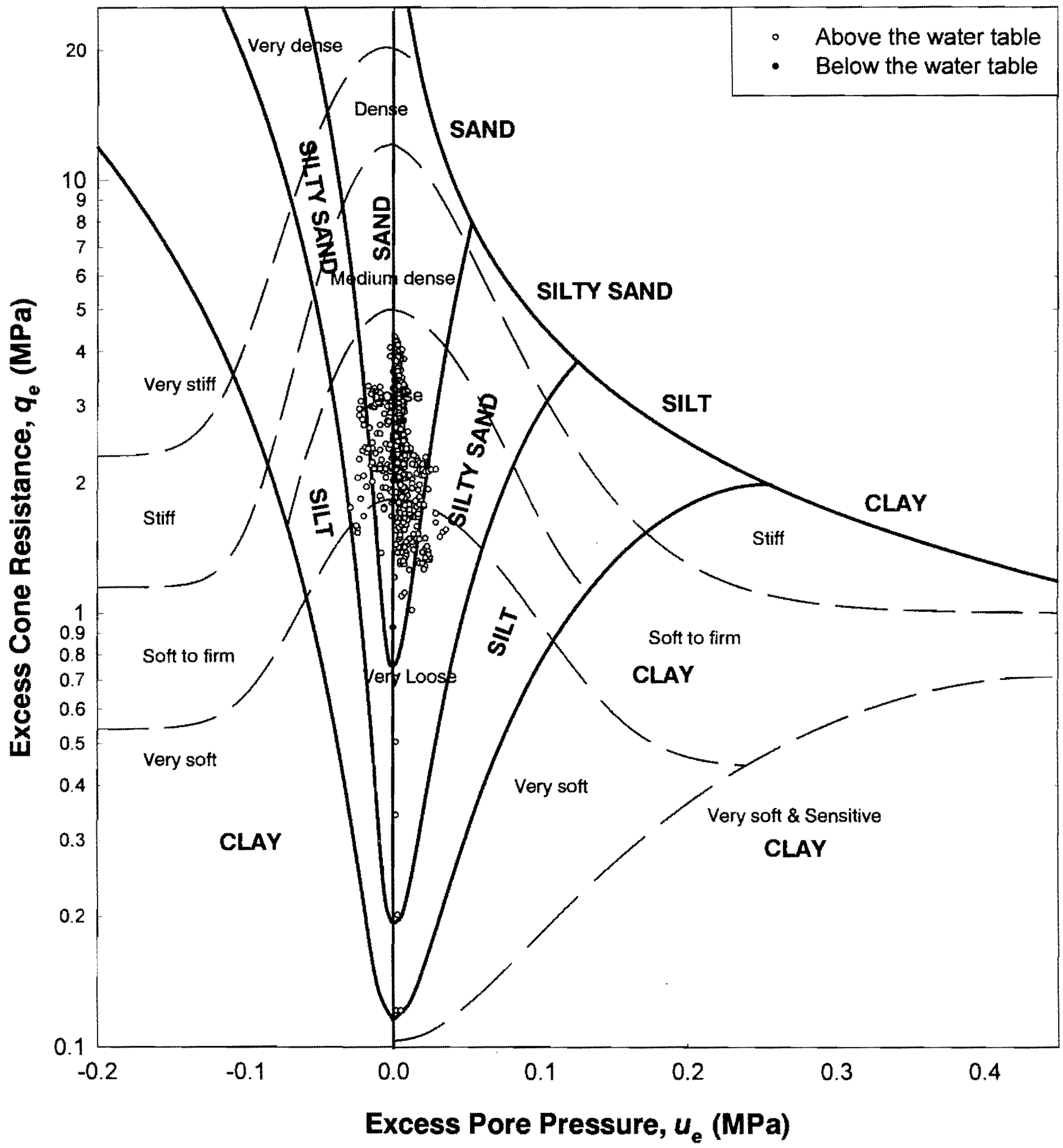


**Figure 4-40: Penetration data for Pay Dam Beach represented on the soils identification chart.**

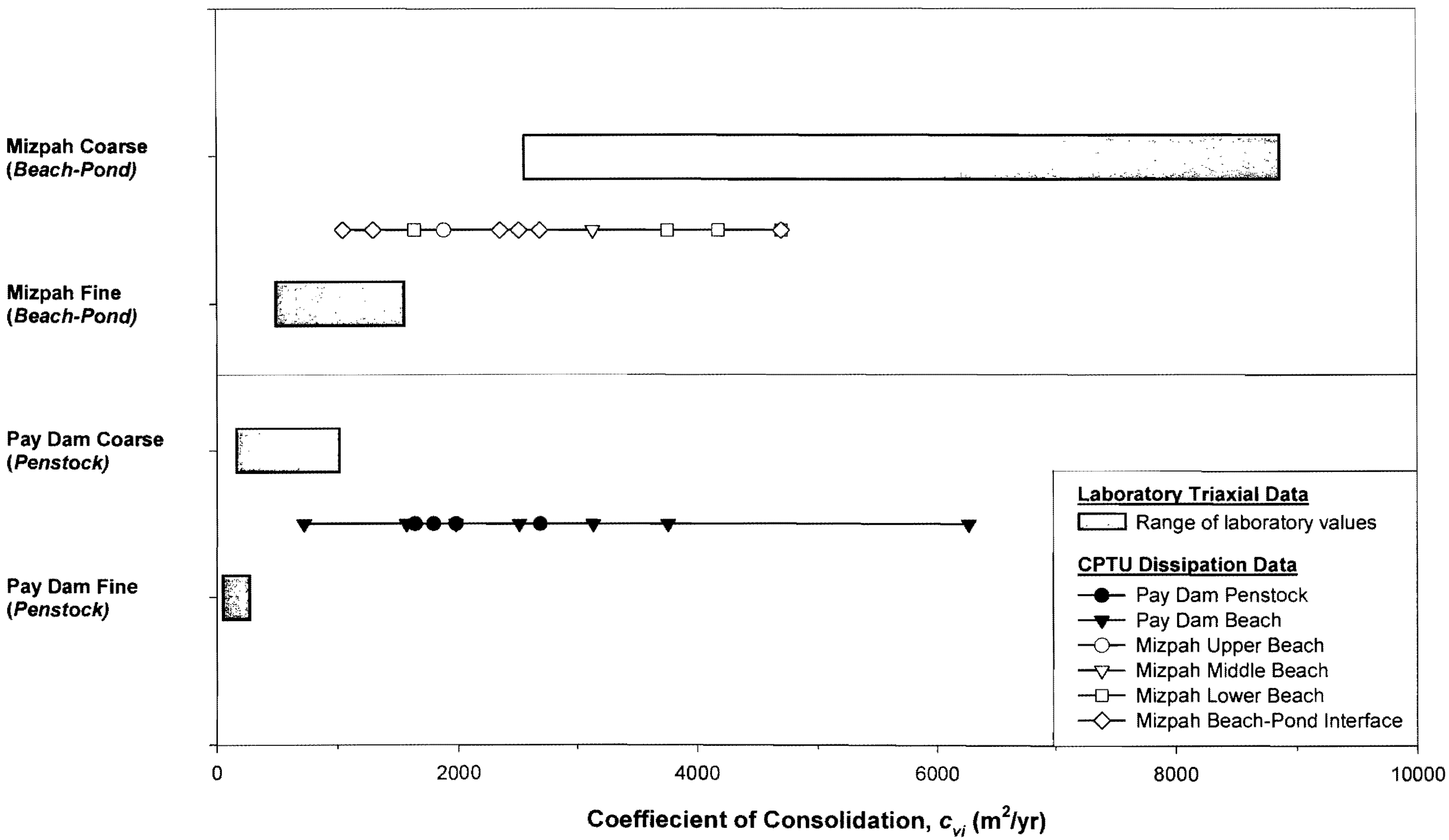


**Figure 4-41: Estimates of the coefficient of consolidation based on Piezocone dissipation tests in Mizpah and Pay Dam.**

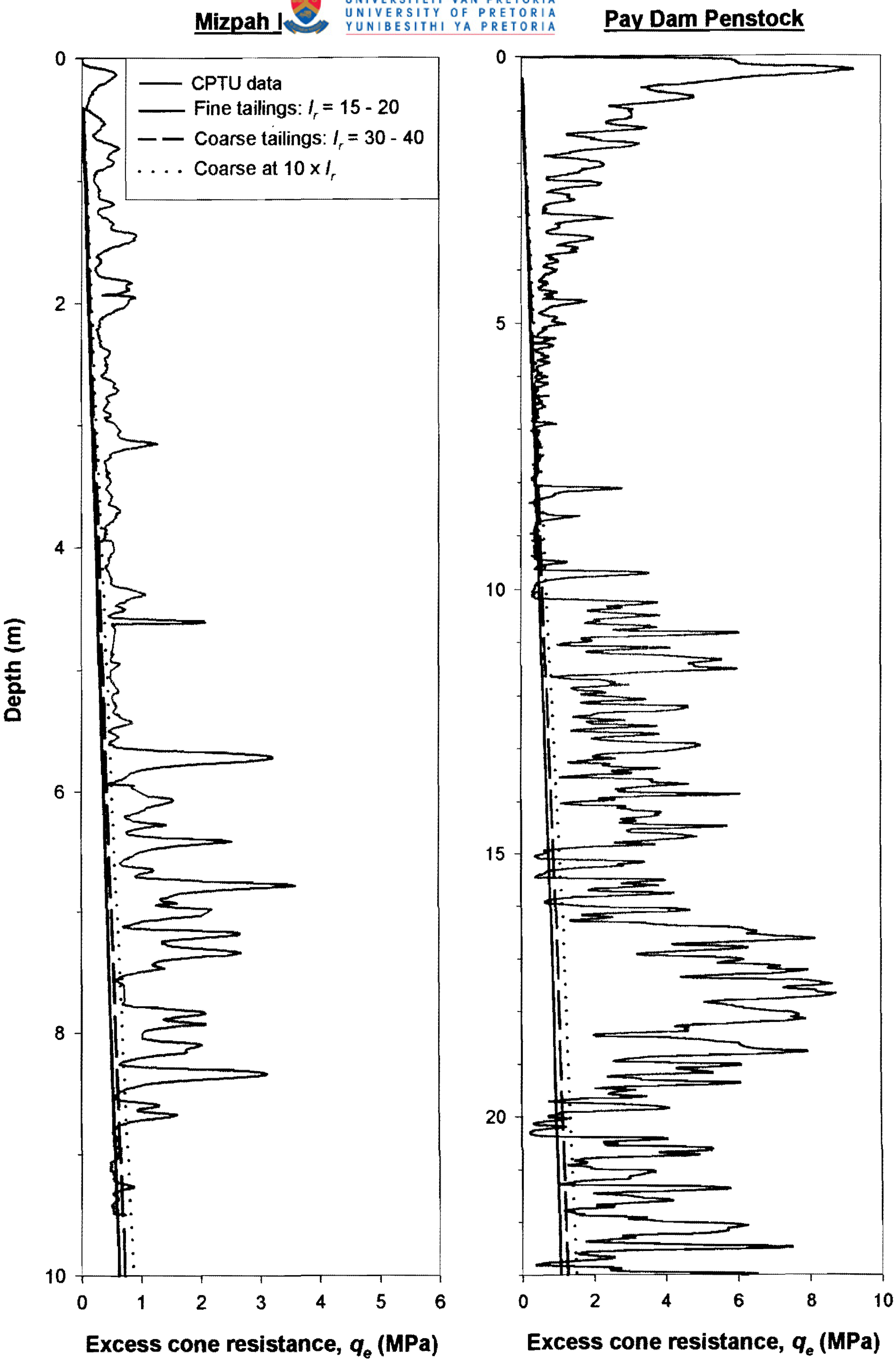


Figure 4-42: Use of cavity expansion theory to model cone penetration in saturated tailings.

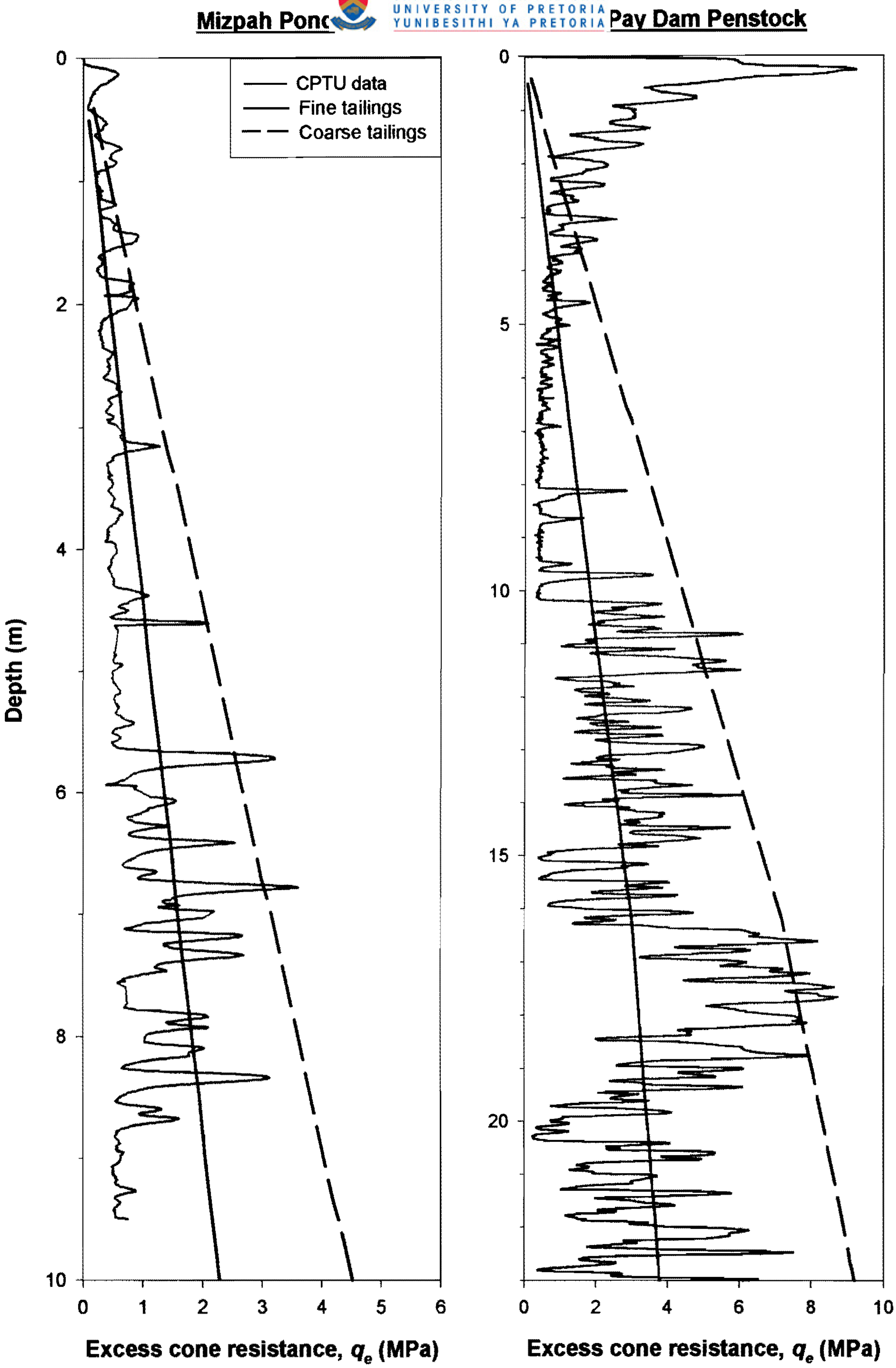


**Figure 4-43: Use of the effective stress formulation proposed by Senneset et.al. (1982; 1988) to model the CPTU in tailings.**

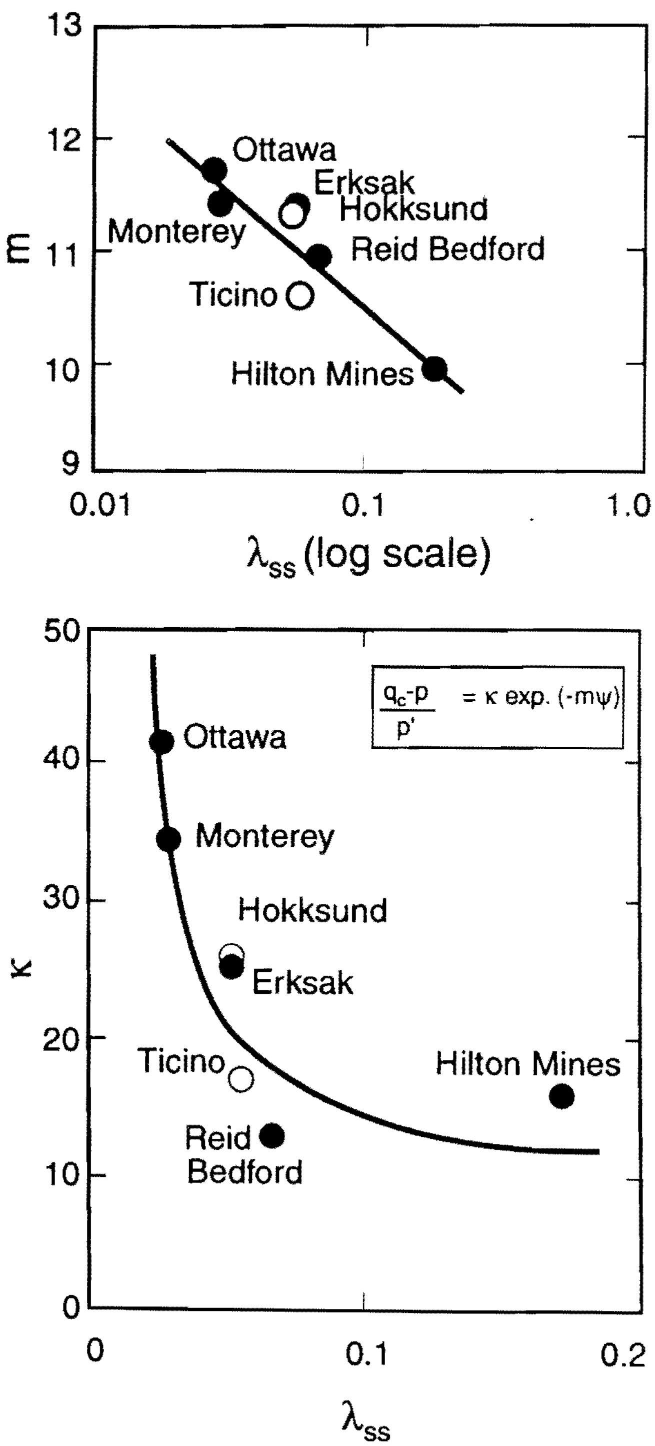


**Figure 4-44: Normalised state parameters κ and *m* (Been et.al., 1986).**

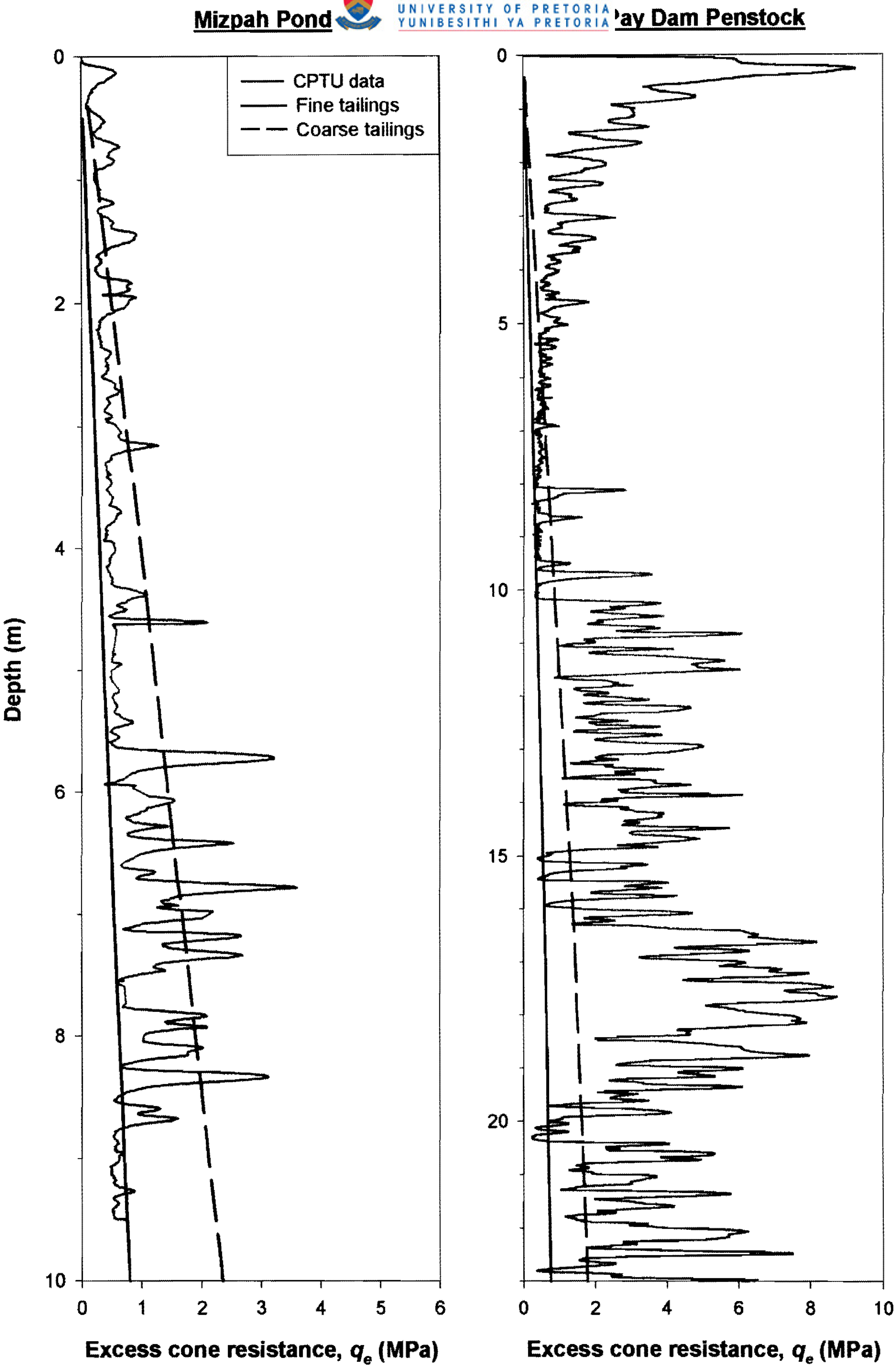


**Figure 4-45: Use of the state parameter approach proposed by Been et.al. (1985) to model the CPTU in tailings.**

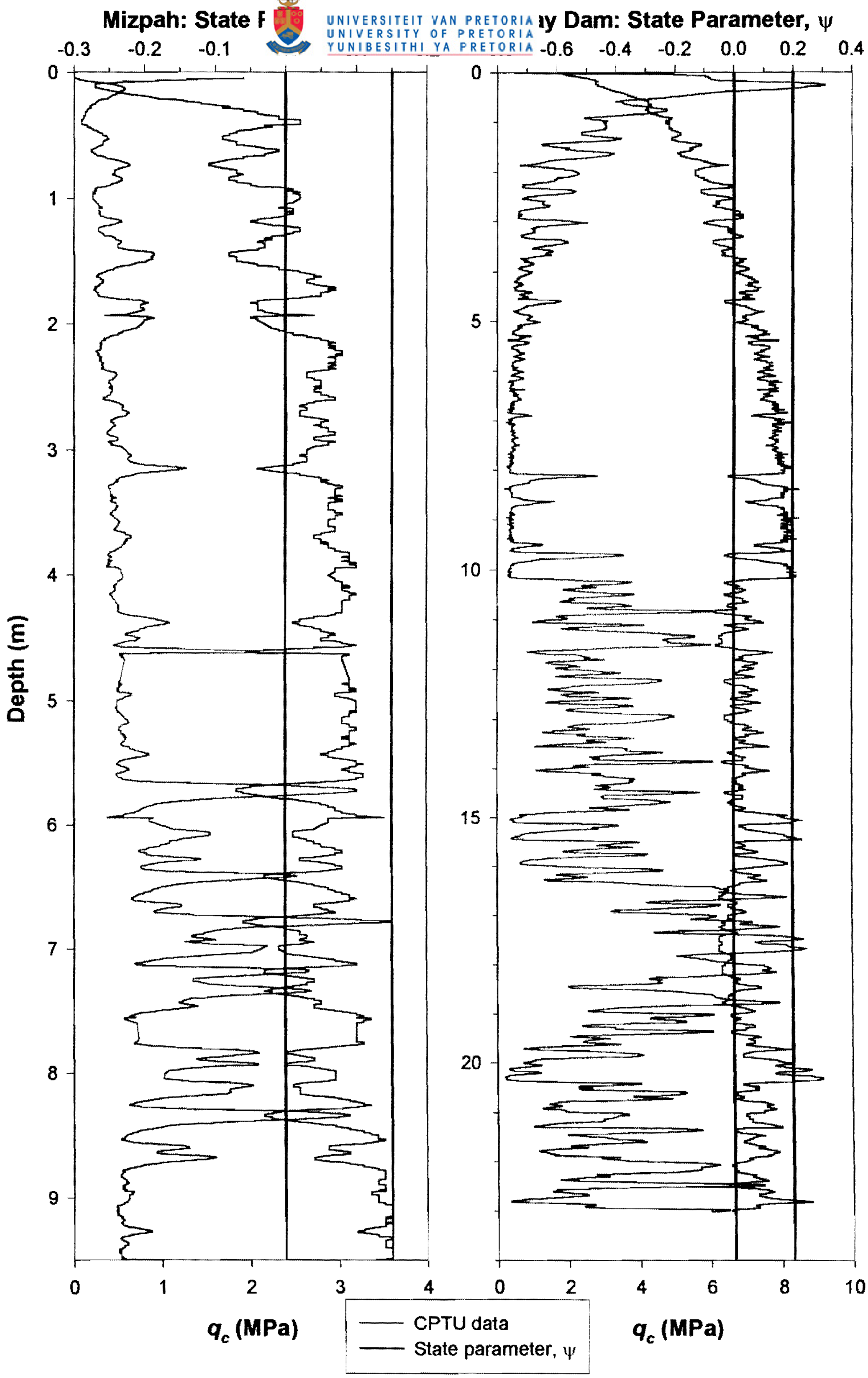


**Figure 4-46: State parameter values from field penetration data.**

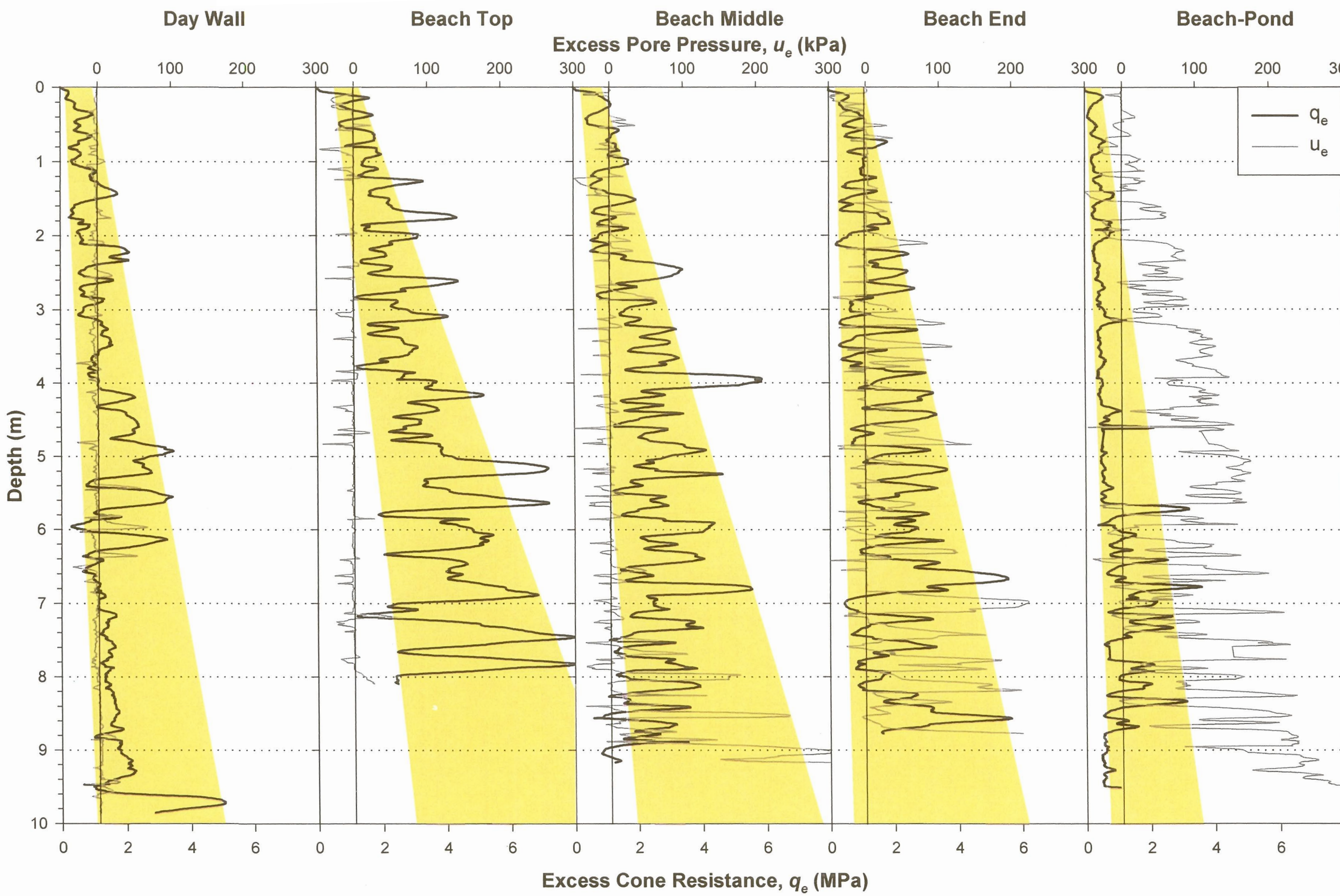


**Figure 4-47: CPTU cross section of Mizpah highlighting the lower and upper boundary cone resistance measurements.**